Paramagnetic singularities of the orbital magnetism in graphene with a Moiré potential

J. Vallejo Bustamante, R. Ribeiro-Palau, C. Fermon, M. Pannetier-Lecoeur, K. Watanabe, T. Tanigushi, R. Deblock, S. Gueron, M. Ferrier, J. N. Fuchs, et al.

Paramagnetic singularities of the orbital magnetism in graphene with a moiré potential

J. Vallejo Bustamante,[1] R. Ribeiro-Palau,[2] C. Fermon,[3] M. Pannetier-Lecoeur,[3] K. Watanabe,[4] T. Tanigushi,[5] R. Deblock,[1] S. Guéron,[1] M. Ferrier,[1] J.N. Fuchs,[6] G. Montambaux,[1] F. Piéchon,[1] and H. Bouchiat[1]

[1]*Université Paris-Saclay, CNRS, Laboratoire de Physique des Solides, 91405 Orsay, France.*
[2]*Université Paris-Saclay, CNRS, C2N, 91120 Palaiseau, France.*
[3]*SPEC, CEA, CNRS, Université Paris-Saclay, 91191 Gif-sur-Yvette, France.*
[4] *Research Center for Functional Materials, National Institute for Materials Science, 1-1 Namiki, Tsukuba 305-0044, Japan*
[5]*International Center for Materials Nanoarchitectonics, National Institute for Materials Science, 1-1 Namiki, Tsukuba 305-0044, Japan*
[6]*Sorbonne Université, CNRS, Laboratoire de Physique Théorique de la Matière Condensée, LPTMC, 75005 Paris, France*

(Dated: April 4, 2023)

The recent detection of the singular diamagnetism of Dirac electrons in a single graphene layer paved a new way of probing 2D quantum materials through the measurement of equilibrium orbital currents which cannot be accessed in usual transport experiments. Among the theoretical predictions is an intriguing orbital paramagnetism at saddle points of the dispersion relation. Here we present magnetisation measurements in graphene monolayers aligned on hexagonal boron nitride (hBN) crystals. Beside the sharp diamagnetic McClure response at the Dirac point, we detect extra diamagnetic singularities at the satellite Dirac points (sDP) of the moiré lattice. Surrounding these diamagnetic satellite peaks, we also observe paramagnetic peaks located at the chemical potential of the saddle points of the graphene moiré band structure and relate them to the presence of van Hove logarithmic singularities in the density of states. These findings reveal the long ago predicted anomalous paramagnetic orbital response in 2D systems when the Fermi energy is tuned to the vicinity of saddle points.

PACS numbers:

Landau diamagnetism originates from the quantum orbital motion of delocalised electrons at low magnetic field. In systems with a periodic potential, this orbital magnetism depends on the specific properties of the lattice.The orbital susceptibility of a single band system is proportional to the curvature of the energy dispersion relation (i.e. the inverse effective mass of carriers). This is known as the Landau-Peierls result [1, 2]. In multiband systems, the coupling induced by the magnetic field between Bloch wavefunctions of different bands gives rise to new effects. The zero field susceptibility is then not only determined by the curvature of the bands, but also by geometrical properties of Bloch functions such as the Berry curvature in reciprocal space [3, 4, 6]. For instance, a divergent diamagnetism of graphene at the Dirac point (DP), (the touching point between electron and hole cone shaped bands) was predicted by McClure [7] and linked to the anomalous π Berry phase which leads to a zero energy Landau level in magnetic field [8, 9].

It was also predicted that orbital magnetism can be paramagnetic rather than diamagnetic. In particular, graphene is expected to exhibit two paramagnetic characteristics: i) a paramagnetic plateau [4–6, 10] on either side of the Dirac point; and ii) logarithmic paramagnetic divergences when the Fermi energy coincides with saddle points of the graphene band structure [4], see Fig.1A. Such paramagnetic orbital susceptibility peaks proportional to the van Hove (vH) singularities in the density of states (DOS) $\rho(\epsilon)$, were predicted long ago at saddle points of the band structure of any 2D crystalline materials by Vignale [11]. A simple physical explanation of the paramagnetic sign lies in the opposite signs of effective masses m_x and m_y at the saddle points

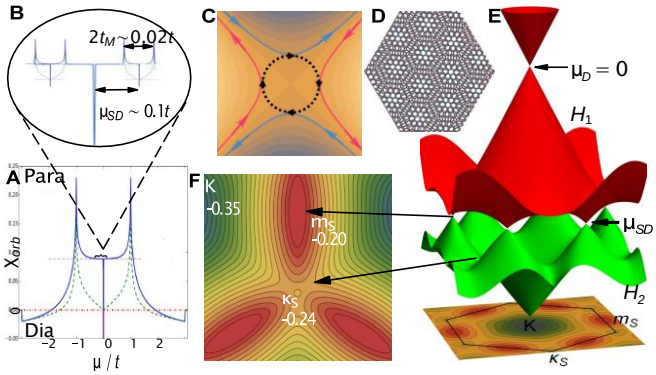

FIG. 1: (**A**) Orbital susceptibility of graphene. Diamagnetic divergent susceptibility is expected at $\mu = 0$ and paramagnetic divergences at the saddle points at $\mu = \pm t$, (adapted from [5]). (**B**) Qualitative expectation of the orbital susceptibility of a graphene/hBN moiré at low energy as a function of the chemical potential. (**C**) Explanation of the existence of paramagnetic currents in the reciprocal space close to a saddle point in a 2D crystal (adapted from [11]). (**D**) Schematic representation of a moiré lattice obtained with the superposition of two honeycomb lattices of different periods. (**E**) Mini-band structure obtained from the diagonalisation of the low energy hamiltonian of graphene in the presence of a moiré potential of amplitude $t_M = -23$ meV. The two highest energy hole bands are represented below the main graphene Dirac point. They display satellite Dirac points at the m_S points of the mini-Brillouin zone. (**F**) Iso-energy lines of the lowest hole band (H_2), a small dip surrounded by 3 saddle points is identified at the κ_S point with C_3 symmetry.

and the fact that the Landau-Peierls susceptibility is proportional to $-\rho(\epsilon)/m_x m_y$. In a magnetic field, near a saddle point, carriers follows hyperbolic-like trajectories in recipro-

cal space. Tunneling between these trajectories (also called magnetic breakdown [12]) gives rise to reconstructed quasi-circular paramagnetic trajectories around the saddle points, see Fig.1C. Reaching these saddle points in pure graphene requires doping to unattainable Fermi levels of the order of the nearest neighbor hopping energy $t = 2.7$ eV. However, in the following we show how, by inducing a large wavelength moiré periodicity in graphene aligned to a hexagonal boron nitride crystal (hBN), we can reach such saddle points in the moiré band structure at reasonable doping and detect the expected singular paramagnetic orbital response.

Due to the small difference between hBN and graphene lattice parameters, the moiré lattice parameter a_M of graphene aligned on hBN, is much larger than the size of the unit cell of graphene (see Fig. 1D). The large period moiré potential leads to the formation of low energy minibands centered on each Dirac point (see Fig. 1E), and the occurrence of low energy satellite Dirac points (at $\mu_{SD} \approx \pm t/10$). These sDPs , accessible by applying moderate gate voltages, were observed experimentally by several groups including [13–17]. They are surrounded by saddle points whose associated vH singularities were detected via DOS measurements [13]. Saddle points were also revealed in electron focusing experiments [18] and more indirectly in magnetic field dependent patterns in Josephson junctions [19]. Field dependent peaks in photoemission spectra [20] as well as in thermoelectric Hall measurements [21] were interpreted as related to orbital magnetisation peaks at those low energy vH singularities.

In this letter we present direct magnetisation measurements on graphene/hBN moiré samples in a wide range of chemical potential. Our experiments reveal the paramagnetic susceptibility singularities predicted long ago at saddle points of the moiré dispersion relation.

Moiré samples and magnetic detection

In order to reach the satellite Dirac points and the neighboring saddle points at moderate doping, we fabricated samples where the hBN and graphene lattices are nearly aligned, leading to the maximum value of the G/hBN moiré superlattice parameter as described in SM. We investigated two different samples, M_A and M_B. Raman spectroscopy was used to verify the alignment (see SM and [17, 22]) and determine the lattice parameters yielding $a_{M_A} = 9.5 \pm 0.5$ nm and $a_{M_B} = 12.5 \pm 0.5$ nm corresponding to 1° and 0.6° mismatch angles respectively.

The magnetisation experiments were performed using the technique described in [23]. The encapsulated samples are deposited on a magnetic field detector based on a pair of highly sensitive giant magnetoresistance (GMR) probes [24–26]. The key point of using these sensors is that whereas the orbital magnetism in the system is generated in response to the out-of-plane external field, the GMRs are only sensitive to the in-plane components of the stray field created by the orbital currents. Connecting the two GMR strips in a Wheatstone bridge configuration and modulating the DC gate voltage, V_g, with an AC bias (Fig.2C), eliminates most of the extraneous spurious magnetic contributions. In this way, one obtains the

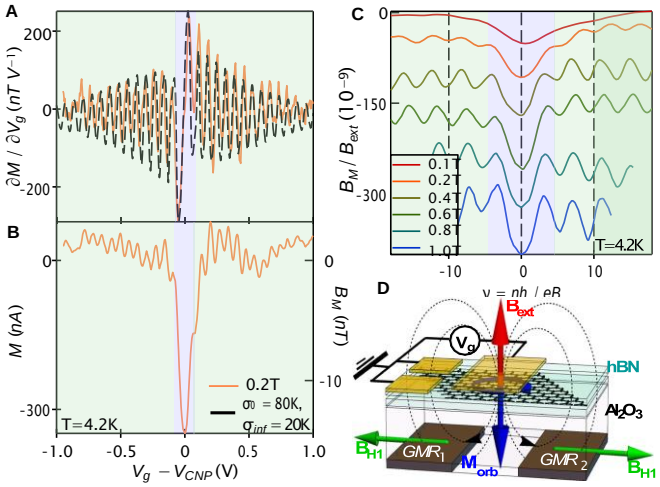

FIG. 2: Low doping data on sample M_A. **(A)** Solid line: derivative of the magnetic field detected by the GMR detector as a function of the gate voltage V_g close to the DP at $B = 0.2$ T. The curve is the average of 10 independent measurements. Dashed line: theoretical gate dependence of $\partial M/\partial V_g$. The disorder amplitudes σ_0 and σ_∞ were determined from the width of the McClure Dirac and the decay of dHVA oscillations. They are respectively 80 K and 20 K . **(B)** Magnetization per unit surface obtained by integration of the data in (A) with, on right axis, units of the equivalent measured magnetic field by the GMR detector. **(C)** Evolution of the McClure peak and dHvA oscillations for different applied out-of-plane magnetic fields. On the y axis the detected magnetic signal on the GMR detector is normalized by the applied field. On the x axis $\nu = n\Phi_0/B$ is the Landau levels filling factor where n is the carrier density.(The apparent increase of χ with B at low field is an artefact due to the gate voltage modulation which broadens the McClure peak. This effect becomes negligible when the intrinsic McClure peak broadening, proportional to B, exceeds the gate voltage modulation.) **(D)** Sketch of the experimental setup. The orbital magnetisation is detected by the voltage between the two dc current biased GMR detectors R_1 and R_2 measured by a lock-in amplifier at the modulation frequency of the gate voltage.

V_g derivative of the magnetisation of graphene area below the gate between the GMR probes. Additional electrodes outside the GMR detection region allow for transport measurements and an independent determination of the main and satellite Dirac points positions. For an applied out-of-plane magnetic field of 0.1 T, the in-plane sensitivity of GMRs sensors coupled to M_A and M_B is respectively 2.5 and 1 Ω/mT and their field equivalent noise is about 1nT/$\sqrt{Hz}$.

Main Dirac point region: McClure peak and de Haas-van Alphen oscillations.

As shown in Fig.2 the magnetisation close to Dirac or charge neutrality point (CNP) features the diamagnetic McClure peak [23]. This peak broadens with out-of-plane magnetic field field and de Haas-van Alphen (dHvA) oscillations appear with increasing doping. Fig.2 shows both the derivative of the magnetisation and the integrated curve as a function of the gate voltage for sample M_A , in a out-of-plane magnetic field of 0.2 T. The amplitude of the detected signal B_M is 15 nT at the DP. This data can be precisely described

deriving the magnetisation from the field dependence of the grand potential of graphene at a chemical potential fixed by the gate voltage [23]. The Landau energy levels in graphene are $\epsilon_N = \pm\sqrt{N}\epsilon_B$ with $\epsilon_B = \sqrt{2ev^2kB}$, where v is the Fermi velocity and N is an integer [7]. Disorder is modeled by a gaussian distribution of chemical potential μ whose standard deviation σ_μ decreases at high doping, due to screening effects which are more efficient. The magnetisation was shown to be a universal function of the variables μ/ϵ_B and σ/ϵ_B. The McClure peak at low field has a width $\sigma_0 = 80 \pm 5$ K at the CNP. dHvA oscillations observed at larger doping exhibit a characteristic energy scale of $\sigma_\infty = 20$ K. Both σ_0 and σ_∞ are twice smaller than in our previous work [23] and indicate a better quality of the present samples. The dashed curve in Fig.2A is the theoretical fit for $\partial M/\partial V_g$ using those parameters. Fig.2C shows the evolution of the magnetisation with Landau level filling factor for different field values. The magnetisation is renormalized by the applied magnetic field, which in the linear regime is the magnetic susceptibility $\chi = M/B$. One notes the increased dHvA oscillations relative to the McClure response as magnetic field increases.

Satellite Dirac points, diamagnetic and paramagnetic singularities.

We now turn to the higher doping regime. Fig.3A shows the four-terminal resistance of sample M_A in a wide range of gate voltage at 4 K. Both satellite peaks are clearly visible at -16 V and 15.5 V from the CNP. Fig.3B, shows the magnetisation response at 0.2 T in the same range of gate voltage, using a 100 mV modulation of the gate voltage. This strong V_g modulation increases the detection sensitivity at high gate voltage but, because the chemical potential scales as $\sqrt{V_g}$, damps the previously discussed diamagnetic McClure response and dHvA oscillations. In the high doping region of interest here, in particular in the region where the sDPs are found in the resistance measurement, we find a series of three antisymmetric peaks, compatible with the expected moiré band orbital magnetism as shown below. The integrated trace displayed in Fig. 3C features a diamagnetic peak (red arrow) in the hole doped region at $V_g - V_{CNP} = 17$ V surrounded by two paramagnetic peaks (black arrows). In the electron doped region, we find similar features showing though somehow different positions of the peaks with an asymmetry in the position of the two paramagnetic peaks with respect to the diamagnetic one. From the value of moiré lattice parameter we find that the gate voltage positions of the diamagnetic peaks correspond, as expected, to a carrier density of 4 n_0 where n_0 is the number of carriers per moiré cell, (the factor 4 comes from spin and valley degeneracies). The peak positions differ slightly from those observed on the resistance measurements shown in Fig.3A, a discrepancy we attribute to the different sample region probed in the resistance measurements [27]. We assign the paramagnetic peaks to the expected magnetic orbital response at the saddle points of the moiré miniband structure. *This is the main result of our letter*. Using the gate capacitance of sample M_A, we determine the energy splitting between the paramagnetic and diamagnetic peaks and therefore

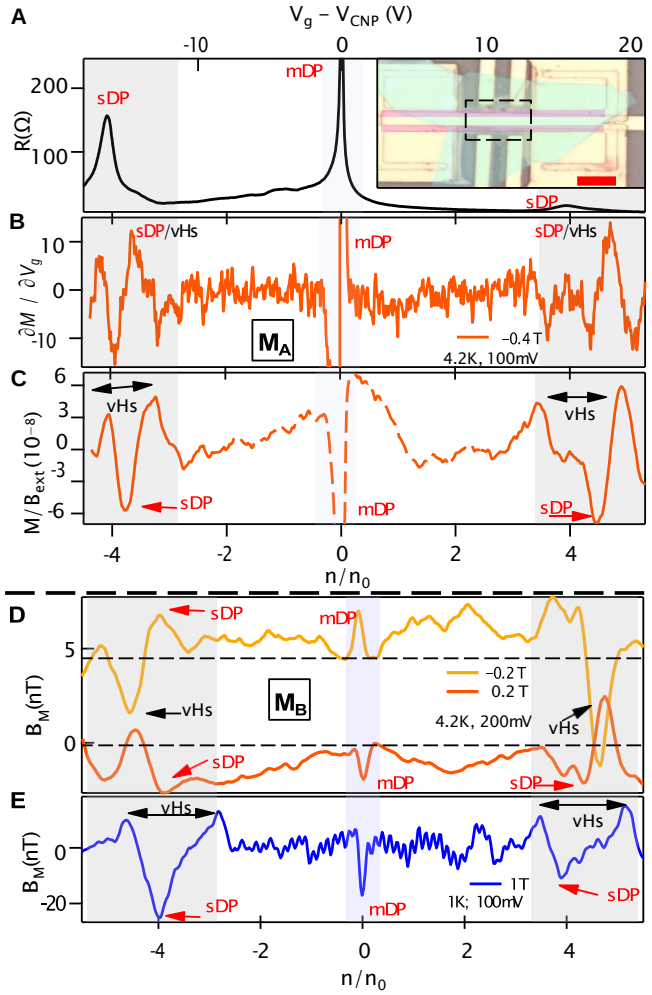

FIG. 3: **(A)** 4 terminal resistance of sample M_A. Inset: optical image of the sample M_A on the top of the GMR detector (red scale bar is 10 μ m). **(B)** Derivative of the magnetisation as a function of the gate voltage and carrier density (renormalised to the moiré filling factor n_0) for a wide doping range in an external magnetic field of 0.2 T for the same sample. **(C)** Magnetization (in units of the magnetic field detected on the GMRs, renormalised by the out-of-plane applied field) obtained by integration of the data in (B). In the region of the secondary Dirac peaks we observe diamagnetic peaks (red arrows) surrounded by paramagnetic peaks (black arrows). **(D,E)** GMR data measured on sample M_B. Numerically integrated magnetisation as a function of the carrier density (renormalised to n_0) at $\pm$0.2 T **(D)** and 1 T, **(E)**.

the expected positions of the vHs, to be in the range of 10 to 20 meV. This yields an estimate of the amplitude t_M of the moiré potential (see Fig.1B), as will be discussed more precisely below.

Fig.3D and 3E also presents equivalent data on sample M_B. At high hole and electron doping one identifies several peaks of similar amplitude. The position of the diamagnetic satellite peaks are consistent with transport data (shown in SM) and with a moiré period larger than that of sample M_A. There as well, HvA oscillations are attenuated by the gate voltage mod-

ulation of 100 mV and invisible at ± 0.2 T, but are visible at 1 T due to their larger period. The data taken, at ± 0.2 T display peaks of opposite sign, approximately at the same positions and with 5 times smaller amplitude than the 1 T data which is consistent with a linear field dependent magnetisation. However, whereas one observes clearly diamagnetic satellite Dirac peaks and outer paramagnetic peaks, in contrast with the data on M_A the inner smaller paramagnetic peaks are nearly undetectable at ± 0.2 T whereas they are visible at 1T. We note that the magnetic energy scale ϵ_B is equal to 30 meV at 1 T i.e. of the order of the moiré potential, which means that the miniband spectrum is modified in a non perturbative way at this field. This can explain why the data at 1 T is significantly different from the the lower field data. In the following, we discuss explanations for the asymmetry in amplitude of paramagnetic singularities on either side of satellite Dirac peaks.

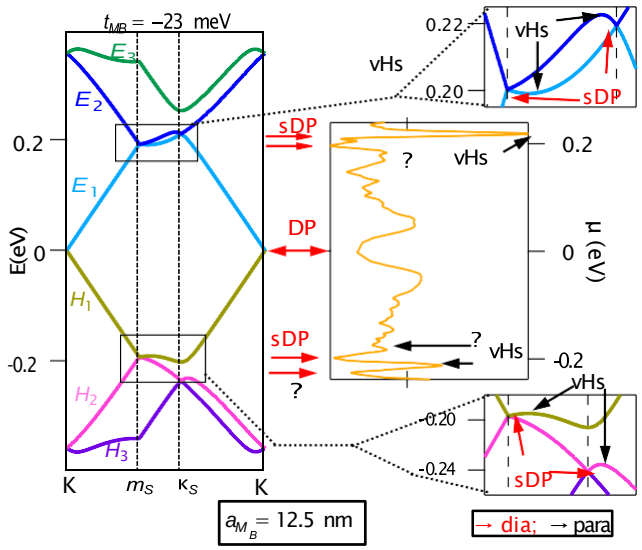

FIG. 4: Comparison between band structure (left) and experimental data for sample M_B (right). We present cuts along the three K, m_S, m_S, κ_S, and κ_S, K axes of the moiré band structure calculated for $t_M = -23 meV$ matching the position of the observed diamagnetic peaks (red arrows) and paramagnetic peaks (black arrows) in magnetisation data function of the chemical potential.

Comparison with a simple theoretical model

Computations of moiré spectra rely on specific modelisations of the moiré potential [13, 28–30]. We use the simplest model which reproduces the positions and amplitudes of the susceptibility peaks at the Dirac and saddle points.This model, initially derived in [13], assumes a C_6-symmetric moiré potential of amplitude t_M which only depends on the positions of carbon atoms with respect to the hBN atoms. We neglect all contributions breaking the inversion symmetry of the graphene lattice such as considered in [20, 29]. The miniband spectrum, folded into the moiré Brillouin zone, can be easily calculated within this approximation as shown in Fig.1, Fig.4 and SM. The amplitude of the moiré potential determines the number of satellite peaks and their position in the momentum space as well as the symmetry of the saddle points. These features also depend on the minibands considered and the type of carriers, electrons or holes, see [13, 20, 29] and theoretical discussion in the SM. When increasing the amplitude t_M of the moiré potential, one finds a clear electron-hole asymmetry of the minibands spectrum determined by the sign of t_M. This is illustrated in Fig.4 showing cuts along the K, κ_S, m_S, K axis of the three lowest moiré electron and highest hole bands around the main DP. For negative values of t_M, the moiré minibands are found to be wider on the hole side compared to the electron side. Whereas crossings occur essentially between the first and the second bands on the electron side, they also occur between the second and third bands on the hole side. These crossings determine the number and position of the satellite Dirac points in reciprocal space. When $|t_M|$ is smaller than 25 meV, band crossings occur both at κ_S and m_S points for the first two electron bands (see SM). These sDPs are separated by ordinary named A_1 saddle points with a C_2 symmetry that connect 2 valleys [31].

Coming back to experiments, we determined t_M from the position of the measured diamagnetic and paramagnetic satellite peaks compared to their expected positions in the moiré band structure for both samples. The calculated spectra which best match the experimental positions of the different peaks are obtained for $t_M = -15$ meV and $t_M = -23$ meV for samples M_A and M_B as shown in SM and Fig.4 for sample M_B. Because of these relatively small values of t_M, E_1 and E_2 bands cross both at κ_S and m_S points at different energies, we therefore expect two families of sDPs. This is compatible with the split diamagnetic satellite McClure peak shown in Fig.4 on the electron side. We attribute the larger splittings observed on the hole side to the crossings between H_2 and H_3 bands.

A more careful analysis of the shape and curvature of the minibands Fig.4, in the vicinity of the κ_S and m_S satellite Dirac points (see also SM) helps explain the asymmetry in position and amplitude of the paramagnetic singularities. These are clearly more pronounced on the high doping sides of sDPs. We find that the miniband curvatures at the A_1 saddle points along $[m_S, \kappa_S]$ are much larger in bands bands E_2 and H_2 compared to bands bands E_1 and H_1. As a result the position in energy of the saddle points on the low doping minibands (E_1 and H_1) are very close to the m_S sDP , in contrast with the large doping ones (E_2 and H_2) located further in energy above κ_S . We show in SM I.C and E that these observations explain why the outer paramagnetic peaks are more intense than the inner ones (tending to overlap with the diamagnetic ones at the m_S SDPs), both on electron and hole side. This asymmetry is more pronounced for sample M_B whose moiré potential is larger than for sample M_A.

We also find theoretically that the first hole miniband H_1 below the main Dirac peak does not exhibit a Dirac point at κ_S but instead a broad shallow minimum turning into a plateau for $|t_M| \gtrsim 30$ meV as shown in SM Fig.S3 and can be viewed as the merging of three A_1 saddle points. This is the signature of a C_3 saddle point surrounded by 3 maxima separated by 3 valleys at 120 degrees and characterized by a dispersion rela-

tion varying as a cubic function of the wave-vector (2nd order curvature cancels in all directions, see [31], for the classification of saddle points). In SM I.D we show that at C_3 saddle points, the DOS exhibits a $\delta\mu^{-1/3}$ divergence in contrast with the logarithmic divergence at A_1 saddle points in agreement with [32]. Moreover, since the effective mass diverges, the Landau-Peierls susceptibility is then not simply proportional to the density of states as shown in [11]. The calculation of the susceptibility is more involved, leading to a $\delta\mu^{1/3}$ singularity in contrast with the logarithmic divergence for A_1 saddle points [11].

At present our experiments are not accurate enough to identify precisely the nature of the different saddle points, but we can compare the amplitudes of the measured magnetisation singularities to theoretical predictions. We first estimate both the theoretical and experimental values of ratio r between the diamagnetic peaks at the main and satellite Dirac points. According to [7, 23] the orbital magnetic susceptibility of graphene at the main Dirac point, χ_M, depends on the square of the Fermi velocity v and the disorder standard deviation σ_0 according to:

$$\chi_M = -\frac{\sqrt{2}v^2e^2}{3\sigma_0\pi^{3/2}} \quad (1)$$

It was pointed out in [13] that the satellite Dirac cones (at the m_S points of the moiré hexagonal Brillouin zone) are anisotropic, leading to an effective Fermi velocity: $\sqrt{v_{sx} \times v_{sy}}$. The anisotropic components of the Fermi velocity along the principal axis of the elliptical energy cross sections in the vicinity of sDP are $v_{sx} = v$, the original Fermi velocity of graphene and $v_{sy} = \frac{\sqrt{3}a_M t_M}{2\hbar}$, the reduced transverse velocity originating from the moiré potential. We then assume that the susceptibility, χ_S, at secondary diamagnetic peaks, is similar to the McClure susceptibility of graphene in Eq.1 replacing v by $\sqrt{v_{sx} \times v_{sy}}$ and the amplitude of disorder σ_0 by σ_s, the width of the sDP (of the order of 4±5 0.5 meV). This leads to the susceptibility ratio: $r = 3\chi_S/\chi_M = 3\frac{v_{sy}\sigma_0}{v\sigma_s}$, considering the 3 fold degeneracy of m_s points. We obtain $r = 0.55$ 0±1 for sample M_B to be compared to the experimental one: 0.33±0.1. For these estimations we have not taken into account the proximity in energy between the the sDPs and the saddle points of bands E_1 and H_1 whose magnetic contributions of opposite sign tend to cancel each another (see SM for more details).

Turning to the paramagnetic susceptibility peaks, we show in SM how one can also estimate their amplitude from the miniband spectrum determined in our simple model by the parameters t_M and a_M. The DOS and the susceptibility depend on the curvatures m_x^{-1} = and m_y^{-1} of the energy bands at the saddle points. They are given in the SM for both samples and A_1 saddle points for the bands E_1, E_2, H_1, H_2. These saddle points are strongly anisotropic with much higher curvatures along the y compared to the x axis (along κ_S, m_S). The ratio m_x/m_y depends strongly on the considered bands. As an example, we find that it is about 20 times larger for the E_1, H_1 compared to the E_2, H_2 bands. On the other hand the geometric mean of the curvatures $\alpha = (m_x m_y)^{-1/2}$ is of the order of $10t_M a_M^2/\hbar^2 = 100m^{-1}$ for all investigated bands where m_e is the free electron mass.

In order to go further and compare these findings to the experiments, one also needs to take into account the effect of disorder. Experiments show that the paramagnetic peaks above the sDP in the electron doped region are of the same order of magnitude as the diamagnetic ones at the sDP. We were expecting instead smaller amplitudes due to the weaker logarithmic divergences at the vH singularities compared to the delta peak anomalies at sDPs. However we show in SM that these results can be understood when considering that the disorder induced rounding of the logarithmic paramagnetic magnetisation singularities at saddle points is smaller than for the diamagnetic ones at the sDPs. From the experimental values of the ratio σ_s/t_M and the estimated band curvatures, one finds that the maxima of the paramagnetic magnetisation at A_1 saddle points for the H_2 and the E_2 bands are of the same order of magnitude as the diamagnetic peaks at the sDPs, and larger than the saddle point paramagnetism on H_1 and E_1 bands (reduced by the vicinity of the SDP and barely seen experimentally for sample M_B). We show in SM that it is possible to reproduce at least qualitatively, the energy positions and relative amplitudes of the two diamagnetic and paramagnetic peaks in the vicinity of the the sDPs in the electron doping range.

Finally we note that the large miniband curvatures, due to the large period of the moiré potential, contrast with the curvatures at the saddle points of the original 2D atomic lattice [11] and exclude any sizable contribution of Pauli magnetism at vH singularities. The Pauli susceptibility χ_P is indeed expected to vary as $\chi_P = \mu_B^2 \rho(\epsilon)$ where $\mu_B = e\hbar/2m_e$ is the Bohr magneton, yielding a ratio between the Vignale orbital and Pauli spin susceptibility $\chi_V/\chi_P = m^2/m_x m_y$ of the order of 10^4, whereas this ratio is of the order of 1 for the 2D square lattice.

In conclusion, our measurements of the orbital magnetisation of graphene with a moiré potential show a rich set of singularities of the orbital magnetisation in the vicinity of sDPs. These consist of diamagnetic peaks at the satellite Dirac points surrounded by paramagnetic peaks which can be associated to the van Hove singularities of the DOS at the saddle points of the mini-band structure induced by the moiré potential. These experiments therefore confirm the long standing theoretical predictions of the existence of paramagnetic orbital magnetism in 2D materials at van Hove singularities which, in the case of the graphene/hBN moiré investigated here, exceeds by far the Pauli susceptibility. A natural prolongation of this work would be to measure the orbital magnetisation of bilayer graphene moiré structures also extensively investigated [33, 34] with the possibility to obtain ferromagnetic orbital phases,[35]. It is also interesting that the typical amplitude of the paramagnetic susceptibility peaks we measure is of the same order of magnitude than the values predicted for graphene bilayer moirés close to the magic angle [36]. This

singular paramagnetic orbital magnetism is shown to possibly lead to the emergence of new kinds of correlated phases when the sample is embedded in a quantum electromagnetic cavity. Our results also motivate the extension of this work to graphene twisted bilayers with larger moiré periods in which field periodic orbital currents are expected [37].

Aknowledgements: The authors thank E. Paul of SPEC-CEA for the GMR sensors patterning R.Weil and S. Autier-Laurent of LPS for Nanofabrication and Cryogenic support. They also aknowledge fruitfull discussions with A.Chepelianskii, F. Parmentier, R.Delagrange, D. Mailly, C. Mora, P.Simon and financial support from the BALLISTOP ERC 66566 advanced grant. This work benefited from the C2N micro nanotechnologies platforms and partly supported by the RENATECH network, the General Council of Essonne and the DIM-SIRTEC. R.R.-P. acknowledge the ERC starting grant TWISTRONICS. K.W. and T.T. acknowledge support from JSPS KAKENHI (Grant Numbers 19H05790, 20H00354 and 21H05233).

[1] L. Landau Zeitschrift für Physik 64, 629 (1930).
[2] R. Peierls Zeitschrift für Physik 80,763 (1933).
[3] D. Xiao, M.C. Chang, Q. Niu, *Rev. Mod. Phys.* 82, 1959 (2010).
[4] A. Raoux, M. Morigi, J.N. Fuchs, F. Piéchon, G. Montambaux. *Phys. Rev. Lett.* 112, 026402 (2014).
[5] A. Raoux, F. Piéchon, J.-N. Fuchs, G. Montambaux, *Phys. Rev. B*, 91, 085120 (2015).
[6] Frédéric Piéchon, Arnaud Raoux, Jean-Noël Fuchs, and Gilles Montambaux Phys. Rev. B 94, 134423 (2016).
[7] J. W. McClure, Phys. Rev. 104, 666–671 (1956).
[8] G. P. Mikitik and Yu. V. Sharlai Phys. Rev. Lett. 82, 2147 (1999).
[9] J.N. Fuchs, F. Piéchon, M.O. Goerbig, and G. Montambaux Eur. Phys. J. B 77, 351 (2010).
[10] G. Gómez-Santos and T. Stauber Measurable Lattice Effects on the Charge and Magnetic Response in Graphene Phys. Rev. Lett. 106, 045504 (2011).
[11] G. Vignale, Phys. Rev. Lett., 67, 3, 358, (1991).
[12] M. L. Cohen and L. M. Falicov Phys. Rev. Lett., 7, 231, (1961).
[13] Yankowitz, M., Xue, J., Cormode, D., Sanchez-Yamagishi, J. D., Watanabe, K., Taniguchi, T., ... LeRoy, B. J. Nature physics, 8(5), 382-386, (2012).
[14] Massive Dirac Fermions and Hofstadter Butterfly in a van der Waals Heterostructure B. Hunt, J. D. Sanchez-Yamagishi, A. F. Young, M. Yankowitz, B. J. LeRoy, K. Watanabe, T. Taniguchi, P. Moon, M. Koshino, P. Jarillo-Herrero, R. C. Ashoori Science L 340,1428 (2013).
[15] C. R. Dean, L. Wang, P. Maher, C. Forsythe, F. Ghahari, Y. Gao, J. Katoch, M. Ishigami, P. Moon, M. Koshino, T. Taniguchi, K.Watanabe, K. L. Shepard, J.Hone and P. Kim Nature, L497,599 (2013).
[16] C. R. Woods, L. Britnell, A. Eckmann, R. S. Ma, J. C. Lu, H. M. Guo, X. Lin, G. L. Yu, Y. Cao, R. V. Gorbachev, A.V. Kretinin, J. Park, L. A. Ponomarenko, M. I. Katsnelson, Yu. N. Gornostyrev, K. Watanabe, T. Taniguchi, C. Casiraghi, H. J. Gao, A. K. Geim, K. S. Novoselov Nature Physics 10, 451 (2014).
[17] Ribeiro-Palau, R., Zhang, C., Watanabe, K., Taniguchi, T., Hone, J., Dean, C. R. Science, 361(6403), 690-693 (2018).
[18] Menyoung Lee, John R. Wallbank, Patrick Gallagher, Kenji Watanabe, Takashi Taniguchi, Vladimir I. Fal'ko, and David Goldhaber-Gordon Science, 6307, 1526 (2016).
[19] D. I. Indolese, R. Delagrange, Péter Makk, J. R. Wallbank, K. Wanatabe, T. Taniguchi, and Christian Schonenberger. Physical Review Letters, 121(137701), (2018).
[20] Sanfeng Wu, Lei Wang, You Lai, Wen-Yu Shan, Grant Aivazian1, Xian Zhang, Takashi Taniguchi,Kenji Watanabe, Di Xiao, Cory Dean, James Hone, Zhiqiang Li, Xiaodong Xu Science Advances, 2(5), [e1600002] (2016).
[21] Moriya, R., Kinoshita, K., Crosse, J. A., Watanabe, K., Taniguchi, T., Masubuchi, S., ... Machida, T. Nature communications, 11(1), 1-6. (2020).
[22] A. Eckmann, J. Park, H. Yang, D. Elias, A. S. Mayorov, G. Yu, R. Jalil, K. S. Novoselov, R. V. Gorbachev, M. Lazzeri, A. K. Geim, C. Casiraghi *Nano Lett.* 13(11), 5242-5246 (2013).
[23] Vallejo Bustamante, J., Wu, N. J., Fermon, C., Pannetier-Lecoeur, M., Wakamura, T., Watanabe, K., ... Bouchiat, H. Science, 374(6573), 1399-1402. (2021).
[24] M. N. Baibich, J. M. Broto, A. Fert, F. Nguyen Van Dau, F. Petroff, P. Etienne, G. Creuzet, A. Friederich, J. Chazelas, Phys. Rev. Lett. 61, 2472–2475 (1988).
[25] B. Dieny, V. S. Speriosu, S. S. P. Parkin, B. A. Gurney, D. R. Wilhoit, D. Mauri, Phys. Rev. B 43, 1297–1300 (1991).
[26] P. A. Guitard, R. Ayde, G. Jasmin-Lebras, L. Caruso, M. Pannetier-Lecoeur, C. Fermon, Appl. Phys. Lett. 108, 212405 (2016).
[27] For samples M_A the position in gate voltage of the diamagnetic peaks differ by 2 volts compared to the resistance peaks. This offset which corresponds to a 5% shift in chemical potential can be attributed to the small size of the gate compared to the size of the sample measured in transport.
[28] Moon, P., Koshino, M. Physical Review B, 90(15), 155406. (2014).
[29] Wallbank, J. R., Patel, A. A., Mucha-Kruczyn´ski, M., Geim, A. K., Fal'Ko, V. I., Phys. Rev. B, 87(24), 245408, (2013).
[30] Jung, J., DaSilva, A. M., MacDonald, A. H., Adam, S. Nat. com., 6(1), 1-11. (2015).
[31] N. F. Q. Yuan and L. Fu, Phys. Rev. B **101**, 125120 (2020).
[32] Daniele Guerci, Pascal Simon, Christophe Mora Phys. Rev. Research 4, L012013 (2022).
[33] Guohong Li, A. Luican, J. M. B. Lopes dos Santos, A. H. Castro Neto, A. Reina, J. Kong and E. Y. Andrei Nature Physics 6,109(2010).
[34] Eva Y. Andrei , Dmitri K. Efetov , Pablo Jarillo- Herrero, Allan H. MacDonald, Kin Fai Mak , T. Senthil, Emanuel Tutuc, Ali Yazdani and Andrea F. Young Nature Materials Reviews 6,201(2021).
[35] Sameer Grover, Matan Bocarsly, Aviram Uri, Petr Stepanov, Giorgio Di Battista, Indranil Roy, Jiewen Xiao, Alexander Y Meltzer, Yuri Myasoedov, Keshav Pareek, Kenji Watanabe, Takashi Taniguchi, Binghai Yan, Ady Stern, Erez Berg, Dmitri K Efetov, Eli Zeldov Nature physics 8, 885(2022).
[36] D. Guerci, P. Simon, C. Mora Phys. Rev. B 103, 224436 (2021). Gian Marcello Andolina et al. https ://arxiv.org/pdf/2210.10371.pdf
[37] S.G. Xu, A.I. Berdyugin, P. Kumaravadivel , F. Guinea, R. Krishna Kumar, D.A. Bandurin, S.V. Morozov, W. Kuang, B. Tsim, S. Liu, J.H. Edgar, I.V. Grigorieva, V.I. Fal'ko, M. Kim , A.K. Geim Nature Communication 10,4008(2019).

April 4, 2023

Supplementary material for: Paramagnetic singularities of the orbital magnetism in graphene with a moiré potential

J. Vallejo Bustamante, R. Deblock, S. Guéron, M. Ferrier, G. Montambaux, F. Piéchon, and H. Bouchiat
Université Paris-Saclay, CNRS, Laboratoire de Physique des Solides, 91405 Orsay, France.

R. Ribeiro-Palau
Université Paris-Saclay, CNRS, C2N, 91120 Palaiseau, France.

C. Fermon and M. Pannetier-Lecoeur
SPEC, CEA, CNRS, Université Paris-Saclay, 91191 Gif-sur-Yvette, France.

K. Watanabe
Research Center for Functional Materials, National Institute for Materials Science, 1-1 Namiki, Tsukuba 305-0044, Japan

T. Tanigushi
International Center for Materials Nanoarchitectonics, National Institute for Materials Science, 1-1 Namiki, Tsukuba 305-0044, Japan

J.N. Fuchs
Sorbonne Université, CNRS, Laboratoire de Physique Théorique de la Matière Condensée, LPTMC, 75005 Paris, France

MINI-BAND STRUCTURE OF GRAPHENE WITH A MOIRÉ POTENTIAL

Band structure

In order to investigate the orbital susceptibility of the graphene layer with a moiré potential on the graphene , we develop the approach of Yankowitz et al [1] (see also Wallbank et al [2]) to determine the mini-band structure. We start from a 2D massless Dirac Hamiltonian H_0 representing the unperturbed graphene layer in a single valley (say the K valley) and add a scalar periodic potential V with 6-fold symmetry to represent the effect of the moiré. The total Hamiltonian reads

$$H = H_0 + V = v\boldsymbol{p}\cdot\boldsymbol{\sigma} + \sigma_0 t_M \sum_{m=0}^{5} e^{i\boldsymbol{G}_m\cdot\boldsymbol{r}}, \tag{1}$$

where $\boldsymbol{\sigma}$ are the Pauli matrices describing the sublattice pseudospin of the honeycomb lattice, σ_0 is the 2×2 unit matrix and v is the Fermi velocity of graphene ($v \sim 10^6$ m/s). The moiré potential has an amplitude t_M and depends on reciprocal lattice vectors $\boldsymbol{G}_m = G\{\cos(m\pi/3), \sin(m\pi/3)\}$ with norm $G = \frac{4\pi}{\sqrt{3}a_M}$, where a_M is the moiré-lattice period. The two vectors $\boldsymbol{G}_1$ and $\boldsymbol{G}_2$ form a basis for the reciprocal lattice (see Fig. 1). A negative (resp. positive) t_M means that the potential minima form a triangular (resp. honeycomb) lattice. In the present experiment, a_M is of the order of 10 nm and t_M is estimated to be ~ -25 meV. The momentum operator is the usual $\boldsymbol{p} \to -i\boldsymbol{k}\boldsymbol{\nabla}$ in 2D (but it is shifted such that K now plays the role of the reciprocal space origin Γ_s). We set $k \equiv 1$, $v \equiv 1$ and take $G^{-1} = \frac{\sqrt{3}}{4\pi}a_M \sim 1$ nm as unit length. Therefore, $kvG \sim 0.4$ eV is the unit energy and the only remaining dimensionless parameter is $t_M \sim -0.06$.

Eigenvectors of H_0 are plane wave spinors $|\boldsymbol{k}, s\rangle$ where $s = \pm$ is the sign of the energy $\varepsilon^{(0)}_{\boldsymbol{k},s} = sk$ and $\boldsymbol{k}$ is a wavevector. We write H in the eigenbasis of H_0. The potential has matrix elements:

$$\langle \boldsymbol{k}', s'|V|\boldsymbol{k}, s\rangle = t_M \delta_{s,s'} \sum_m \delta_{\boldsymbol{k}',\boldsymbol{k}+\boldsymbol{G}_m}. \tag{2}$$

As we are only interested in the first few bands (typically the 6 bands closest to zero energy), we truncate the Hilbert space at low energy. For each $\boldsymbol{k}$ in the first Brillouin zone (called moiré or mini Brillouin zone, mBZ, see Fig. 1), we only keep states $|\boldsymbol{k}', s\rangle$ such that $\boldsymbol{k}' - \boldsymbol{k}$ is a reciprocal lattice vector (i.e. $\boldsymbol{k}' - \boldsymbol{k} = c_1\boldsymbol{G}_1 + c_2\boldsymbol{G}_2$ with c_1 and c_2 integers) such that $|\boldsymbol{k}' - \boldsymbol{k}| \le 2$. This means that the energy $|\varepsilon|$ should be smaller than the cutoff $\varepsilon_c = 2$. At positive energy, there are 19 such states, see Fig. 1 showing one central Dirac cone circle in red (of radius 0.55 chosen close to the satellite Dirac points and such as to show intersections between the circles), 6 nearest neighbors in green (first shell) and 12 next-nearest neighbors in blue (second shell).

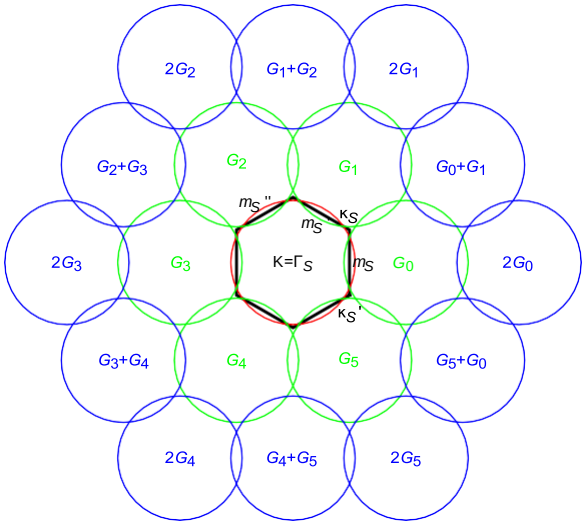

FIG. 1. Truncation in reciprocal space showing a central Dirac cone section (red circle of radius $0.55G$), surrounded by a first shell of 6 green circles and a second shell of 12 blue circles. The mBZ is shown as a black hexagon and high symmetry points are indicated (Γ_S, κ_S with 3-fold degeneracy (C3 symmetry) and m_S with 2-fold degeneracy (C2 degeneracy)). In the limit of vanishing t_M, there is a Dirac point at m_S between the two lowest electron bands and between the two lowest hole bands. Correspondingly at κ_S, there is a 3-fold degeneracy between the three lowest electron bands and between the three lowest hole bands. Dirac points emerge at the three m_S points and unusual C_3 saddle points appear at the two κ_S points.

For each wavevector in the mBZ, we numerically diagonalize the Hamiltonian matrix to obtain 38 bands, of which we only keep the 6 closest to zero energy (3 at positive and 3 at negative energy). As $|t_M| \ll 1$, we are in a regime of nearly-free Dirac electron and the free band structure $\varepsilon^{(0)}_{\boldsymbol{k}} = sk$ should mostly be affected near mBZ edges. Because of truncation in reciprocal space, our calculation is only valid for $|t_M| \ll 1$, which means that we will restrict to $|t_M| \leq 0.1$.

As there is a symmetry between positive and negative energy upon changing the sign of t_M (see Fig. 2, we only discuss $t_M \leq 0$ (typically $t_M \sim -0.05$). We find that, on top of the main Dirac point (crossing of E_1 and H_1, at zero energy and $K = \Gamma_S$), the mini band structure consists of 3 satellite Dirac points (sDP) at m_S between the two lowest bands E_1 and E_2 (at energy $\varepsilon \approx 0.5$) and 2 extra ones at κ_S between E_1 and E_2 (at energy $\varepsilon = 1/\sqrt{3} \approx 0.57$). The two sets of sDP are connected by 6 (in each band) usual A_1 saddle points between m_S and κ_S, see Figs. 2 and 3.

The situation is more subtle on the hole side: there are 3 sDPs at m_S between the two lowest bands H_1 and H_2 (at energy $\varepsilon \approx -0.5$) and 2 extra ones at κ_S between H_2 and H_3 (at energy $\varepsilon = -0.57$). The band H_1 does not touch H_2, but it features a dip (with C_3 symmetry) at κ_S. There are also 6 A_1 saddle points between m_S and κ_S, see Figs. 2 and 3(A,C). The existence of two sets of sDP at nearby energy (-0.5 and -0.57) may explain the observed splitting of the McClure diamagnetic peak. This splitting appears larger on the hole side than on the electron side and may be explained by the fact that the two sets of sDP are between H_1 and H_2 at m_S but between H_2 and H_3 at κ_S.

If we increase t_M up to -0.17 (a value at which our calculations start to suffer from the truncation), we find that three A_1 saddle points merge into an unusual C_3 saddle point at κ_S in the H_1 band, see Fig 3(B). This C_3 saddle point seems to exist for t_M in between -0.14 and -0.25. There are two-fold degeneracies at m_S and κ_S that are never split by t_M and are responsible for the existence of Dirac points.

We show in Fig.4 and Fig.5 contour plots for the different bands E_1, E_2 and H_1, H_2 calculated for t_M =-23 meV, zooming around κ_S and m_S. This data illustrates the strong anisotropy of the saddle points on the H_1 and E_1 bands compared to the H_2 and E_2 bands. We note that the very high estimated values of the curvatures $\alpha_x = 1/m_x$ and $\alpha_y = 1/m_y$ for the E_1 and H_1 bands are only meaningfull in a very small energy range beyond which the bands vary linearly with k. These band structures are expected to be rounded by disorder, leading to smaller effective values of α_y and therefore α.

Analytical approximation

In this section, we construct effective minimal Hamiltonian models near the m_S and κ_S points in the presence of the moiré coupling potential and explore the nature of the saddle points of the first two electron bands $E_{1,2}$ (resp. hole bands $H_{1,2}$) along the line joining m_S to κ_S.

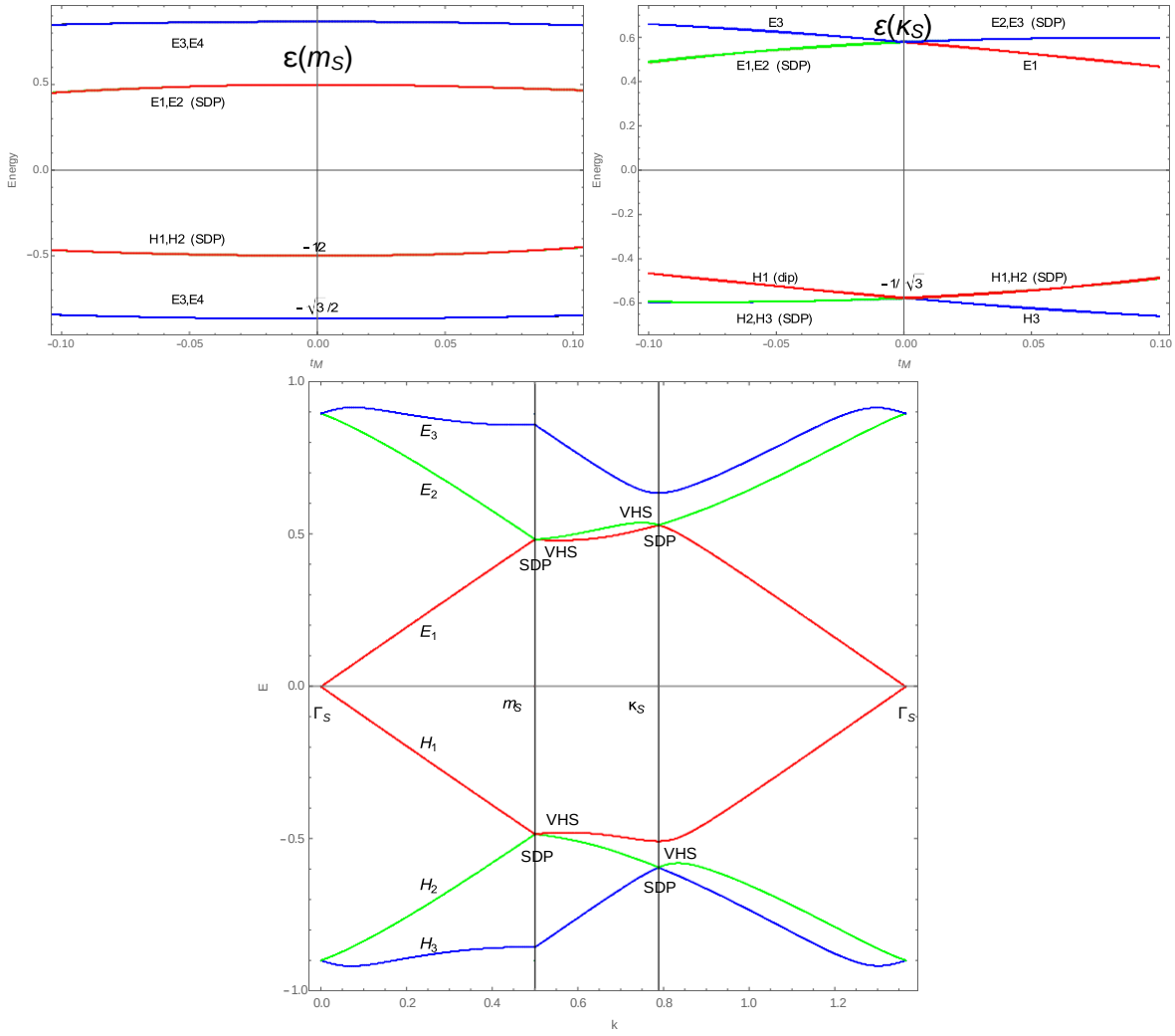

FIG. 2. Upper curves: evolution of the low-energy energy bands at m_S, left and κ_S right as a function of the strength of the moiré potential t_M (in units of $k_v G$). Lower curves:band structure along the closed path $\Gamma_S \to m_S \to \kappa_S \to \Gamma_S$ in reciprocal space (k is a wavevector in units of G) showing the 3 upper hole bands (H_1, H_2, and H_3) and 3 lower electron bands (E_1, E_2, and E_3) for graphene in the presence of a C_6 moiré potential. The moiré potential has a strength $t_M = -0.064$.

Considering the low energy Dirac Hamiltonian $H(\boldsymbol{k}) = k_x\sigma_x + k_y\sigma_y$, the corresponding pseudospin eigenstates $|s, \boldsymbol{k}\rangle$ of energy $\varepsilon^{(0)}_{\boldsymbol{k},s} = s|\boldsymbol{k}|$ may be written as

$$|s, \boldsymbol{k}\rangle = \frac{1}{\sqrt{2}} \begin{pmatrix} s \\ \frac{k_x + ik_y}{|\boldsymbol{k}|} \end{pmatrix}. \tag{3}$$

We can then obtain the overlap matrix between the two eigenstates $|s, \boldsymbol{k}\rangle$ and $|s, \boldsymbol{k}'\rangle$

$$\langle s, \boldsymbol{k}|s, \boldsymbol{k}'\rangle = \frac{1}{2}\left(1 + \frac{\boldsymbol{k}\cdot\boldsymbol{k}'}{|\boldsymbol{k}||\boldsymbol{k}'|} + i\frac{\boldsymbol{k}\times\boldsymbol{k}'}{|\boldsymbol{k}||\boldsymbol{k}'|}\right). \tag{4}$$

Hereafter, since the overlap does not depend on the band index we simply denote $\langle s, \boldsymbol{k}|s, \boldsymbol{k}'\rangle \equiv \langle \boldsymbol{k}|\boldsymbol{k}'\rangle$. For what follows what is needed is the overlap matrix between $\boldsymbol{k}_1 = k\boldsymbol{e}_1 + \boldsymbol{q}$ and $\boldsymbol{k}_2 = k\boldsymbol{e}_2 + \boldsymbol{q}$ with $\boldsymbol{e}_{1,2}$ two distinct unit vectors. To order $\boldsymbol{q}$ one finds,

$$\langle k\boldsymbol{e}_1 + \boldsymbol{q}|k\boldsymbol{e}_2 + \boldsymbol{q}\rangle = \frac{1}{2}(1 + (\boldsymbol{e}_1\cdot\boldsymbol{e}_2 + i\boldsymbol{e}_1\times\boldsymbol{e}_2)(1 - \frac{\boldsymbol{q}\cdot(\boldsymbol{e}_1+\boldsymbol{e}_2)}{k}) + \frac{\boldsymbol{q}\cdot(\boldsymbol{e}_1+\boldsymbol{e}_2)}{k} + i\frac{\boldsymbol{q}\times(\boldsymbol{e}_1-\boldsymbol{e}_2)}{k}); \tag{5}$$

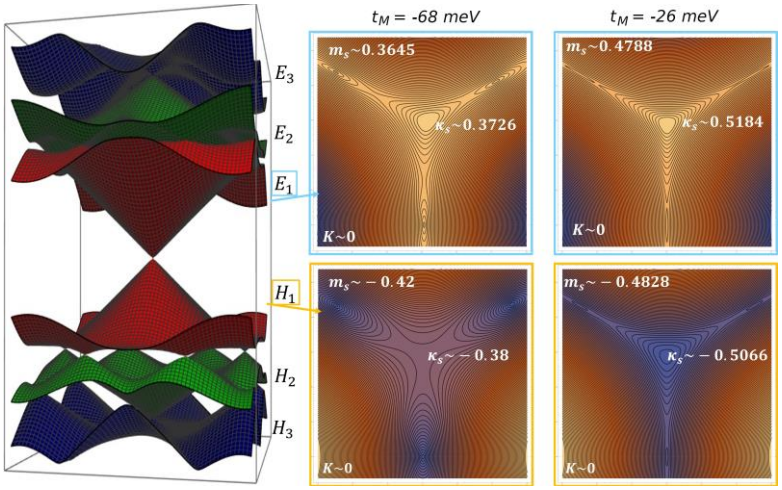

FIG. 3. (Left) 3D plot showing the 3 upper hole bands (H_1, H_2, and H_3) and 3 lower electron bands (E_1, E_2, and E_3) for graphene in the presence of a C_6 moiré potential. (Right) Contour plots of the highest hole band H_1 and lowest electron band E_1 for a moiré potential $t_M = -0.17$ ▪ -68 meV (in units of $\hbar v_F G \sim 0.4$ eV). For H_1, one can notice sDPs at the 3 m_S points and an unusual C_3 saddle point at each κ_S point. At a lower value $t_M = -0.064$ ▪ -26 meV, a dip appears at κ_S in H_1 resulting in the formation of 6 usual A_1 saddle points in between κ_S and m_S. For E_1 and for both values of t_M, there are 3 sDPs at m_S, 2 sDPs at κ_S and 6 A_1 saddle points.

where to order $\boldsymbol{q}^2$ one has

$$|k\boldsymbol{e}_1 + \boldsymbol{q}| = \sqrt{(k^2 + \boldsymbol{q}^2 + 2k\boldsymbol{q}\cdot\boldsymbol{e}_1)} = k + \boldsymbol{q}\cdot\boldsymbol{e}_1 + \frac{(\boldsymbol{q}\times\boldsymbol{e}_1)^2}{2k}. \tag{6}$$

Effective Hamiltonian around m_S

According to Fig. 1, the two bare/primary Dirac points closest to the point m_S are situated at Γ_S and $\mathbf{G}_0$ and verify $\boldsymbol{k}_{m_S} = \Gamma_S + \boldsymbol{k}_+ = \mathbf{G}_0 + \boldsymbol{k}_-$ with $\boldsymbol{k}_\pm = \pm k\boldsymbol{e}_x$ where $k = \frac{1}{2}$ in units of G. Before turning on the moiré potential, around m_S, the two degenerate electron bands $E_{1,2} = k - \frac{1}{2}$ (resp. hole bands $H_{1,2} = -k$) correspond to the states $|s, \boldsymbol{k}_\pm\rangle$ with $s = +$ for electron and $s = -$ for hole.

Turning on the moiré potential, the effective Hamiltonian around m_S that only considers the coupling between the degenerate bands reads (with $|\boldsymbol{q}| \ll 1$)

$$\mathrm{H}_{m_S} = \begin{matrix} s|\boldsymbol{k}_+ + \boldsymbol{q}| & t_M\langle \boldsymbol{k}_+ + \boldsymbol{q}|\boldsymbol{k}_- + \boldsymbol{q}\rangle \\ t_M\langle \boldsymbol{k}_- + \boldsymbol{q}|\boldsymbol{k}_+ + \boldsymbol{q}\rangle & s|\boldsymbol{k}_- + \boldsymbol{q}| \end{matrix}, \tag{7}$$

To correctly describe the energy spectrum at order $\boldsymbol{q}^2$ it is sufficient to take the approximate expressions Eqs. (5, 6), we obtain:

$$\mathrm{H}_{m_S} = s(k + \frac{q^2}{2k})\sigma_0 + sq_x\sigma_z - \frac{t^M}{k}q_y\sigma_y. \tag{8}$$

The last two terms of the above Hamiltonian correspond to an anisotropic Dirac cone at m_S with effective velocities $c_x = |s| = 1$ and $c_y = |t_M|/k = 2|t_M|$.

For $s > 0$ (electron side), one obtains the band dispersions $E_1(\boldsymbol{q}) = k + \frac{q^2}{2k} - \sqrt{q_x^2 + \frac{t_M^2}{k^2}q_y^2}$ and $E_2(\boldsymbol{q}) = k + \frac{q^2}{2k} + \sqrt{q_x^2 + \frac{t_M^2}{k^2}q_y^2}$. The corresponding energy spectrum resembles that of a Rashba Hamiltonian however with an effective strong anisotropy in the Rashba-like coupling. This anisotropy in the Rashba-like coupling appears to be at the origin of the presence of two saddle points in the band $E_1(\boldsymbol{q})$ whereas it is obvious that the band $E_2(\boldsymbol{q})$ has no saddle point. More quantitatively the band $E_1(\boldsymbol{q})$ exhibits a pair of saddle points at postions $\boldsymbol{q}^* = (0, \pm t_M)$ which, as expected, are along the line joining m_S to κ_S. Expanding $E_1(\boldsymbol{q})$ to quadratic order around the saddle points one finds

$$E_1(\boldsymbol{q}^* + \boldsymbol{q}) = k + \frac{(t_M + q_y)^2}{2k} - \sqrt{q_x^2 + \frac{t_M^2}{k^2}(t_M + q_y)^2} \text{ ▪ } E_1^* + \frac{q_y^2}{2m_{yy}} + \frac{q_x^2}{2m_{xx}} \tag{9}$$

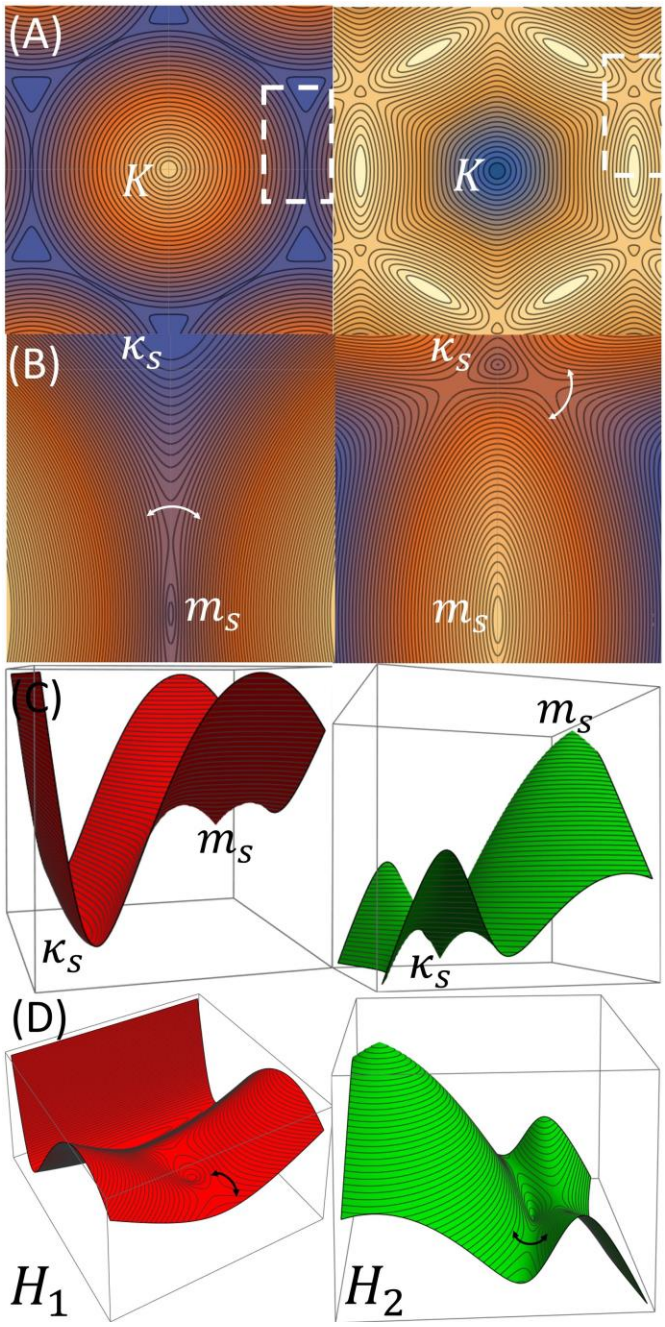

FIG. 4. (A) Contour plot of bands H_2 (left) and H_1 (right) in the mini Brillouin zone. (B) Zoom around κ_s and m_s points. (C) and (D) 3D representation of the bands close to κ_s and m_s. The curved double arrow indicates the saddle point.

with $E_1^* = k - \frac{t^2}{2k}$, $m_{yy} = k$ and $m_{xx} = -\frac{t^2}{k}$. The corresponding curvatures are $\alpha_x = 1/(2m_{xx}) = -1/(2t_M)^2$ and $\alpha_y = 1/(2m_{yy}) = 1$. From these expressions, one deduces that the saddle points energy is shifted by an amount $-\frac{t^2}{2k}$ from the secondary Dirac point at m_s. This energy shift, as well as the negative effective mass m_{xx}, are very small since they are quadratic in the moiré potential strength t_M. This also means that the saddle point is very anisotropic ($|\alpha_x/\alpha_y| = 1/(2t_M)^2 \sim 100$).

For hole bands, since $H_{1,2}(\boldsymbol{q}) = -E_{1,2}(\boldsymbol{q})$, one deduces that only $H_1(\boldsymbol{q})$ exhibits saddle points (at positions $\boldsymbol{q}^* = (0, \pm t_M)$) with energy shift and effective masses opposite to that of $E_1(\boldsymbol{q})$.

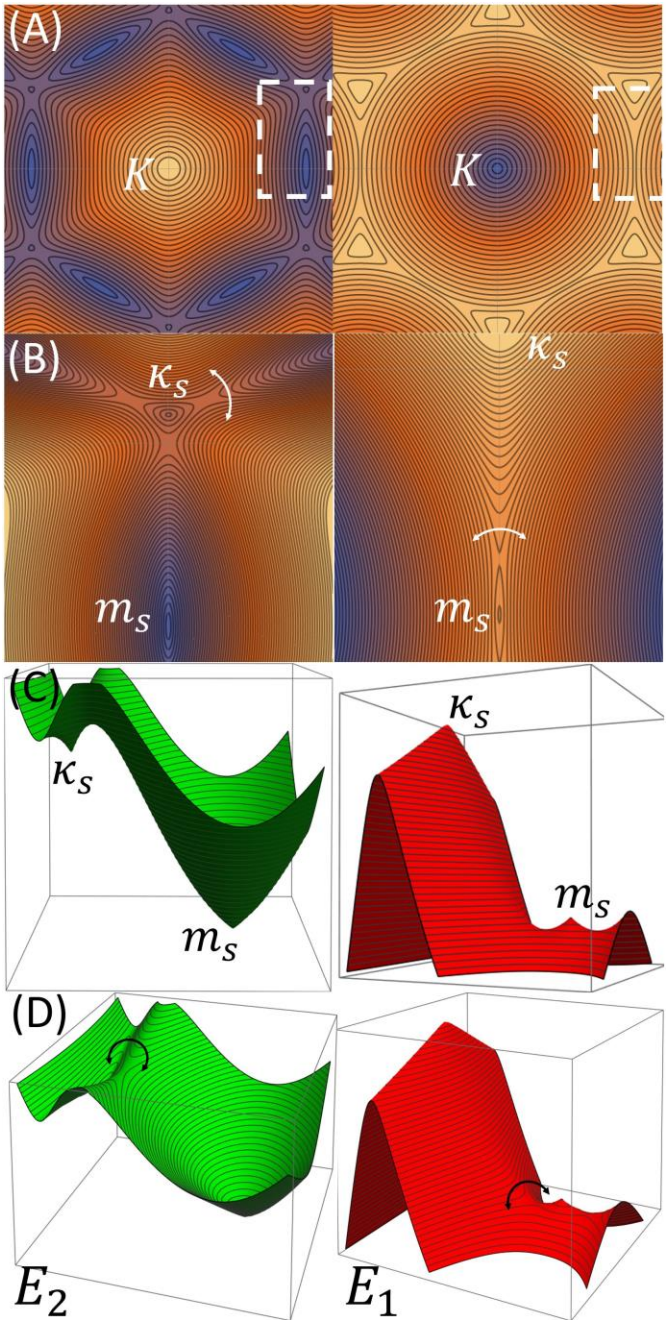

FIG. 5. (A) Contour plot of bands E_1 (left) and E_2 (right) in the mini Brillouin zone. (B) Zoom around κ_s and m_s points. (C) and (D) 3D representation of the bands close to κ_s and m_s. The curved double arrow indicates the saddle point.

Effective Hamiltonian around κ_S

According to Fig. 1, the three bare Dirac points closest to κ_S are situated at positions Γ_S, $\mathbf{G}_0$ and $\mathbf{G}_1$ that verify $\boldsymbol{k}_{\kappa_S} = \Gamma_S + k\boldsymbol{e}_1 = \mathbf{G}_0 + k\boldsymbol{e}_2 = \mathbf{G}_1 + k\boldsymbol{e}_3$, with $k = \frac{1}{\sqrt{3}}$ and $\boldsymbol{e}_1 = \left(\frac{\sqrt{3}}{2}, \frac{1}{2}\right)$, $\boldsymbol{e}_2 = \left(-\frac{\sqrt{3}}{2}, \frac{1}{2}\right)$ and $\boldsymbol{e}_3 = (0, -1)$ such that $\sum_i \boldsymbol{e}_i = 0$. Before turning on the moiré potential there is a three fold degeneracy in bands $E_{1,2,3} = k = \frac{1}{\sqrt{3}}$ (resp. $H_{1,2,3}$) at each κ_S point. These three fold degenerate bands correspond to the states $|s, k\boldsymbol{e}_i\rangle_{i=1,2,3}$ with $s = +$ for electron and $s = -$ for hole. Turning on the moiré potential, the effective Hamiltonian around the point κ_S that only considers the coupling between the degenerate

bands reads (with $|\boldsymbol{q}| \ll 1$)

$$\mathbf{H}_{\kappa_S} = \begin{pmatrix} s|k\boldsymbol{e}_1+\boldsymbol{q}| & t_M\langle k\boldsymbol{e}_1+\boldsymbol{q}|k\boldsymbol{e}_2+\boldsymbol{q}\rangle & t_M\langle k\boldsymbol{e}_1+\boldsymbol{q}|k\boldsymbol{e}_3+\boldsymbol{q}\rangle \\ t_M\langle k\boldsymbol{e}_2+\boldsymbol{q}|k\boldsymbol{e}_1+\boldsymbol{q}\rangle & s|k\boldsymbol{e}_2+\boldsymbol{q}| & t_M\langle k\boldsymbol{e}_2+\boldsymbol{q}|k\boldsymbol{e}_3+\boldsymbol{q}\rangle \\ t_M\langle k\boldsymbol{e}_3+\boldsymbol{q}|k\boldsymbol{e}_1+\boldsymbol{q}\rangle & t_M\langle k\boldsymbol{e}_3+\boldsymbol{q}|s,k\boldsymbol{e}_2+\boldsymbol{q}\rangle & s|k\boldsymbol{e}_3+\boldsymbol{q}| \end{pmatrix}. \tag{10}$$

The above form of the Hamiltonian around κ_S point verifies a C_3 symmetry. As a consequence, up to order $\boldsymbol{q}^2$ the energy spectrum is fully isotropic around κ_S and therefore it cannot exhibits any saddle point to this order. Defining $C_1(\boldsymbol{q}) = \mathrm{Tr}\mathrm{H}_{\kappa_S}/3$, $C_2(\boldsymbol{q}) = \mathrm{Tr}(\mathrm{H}_{\kappa_S} - C_1\mathrm{Id})^2$ and $C_3(\boldsymbol{q}) = \mathrm{Tr}(\mathrm{H}_{\kappa_S} - C_1\mathrm{Id})^3$, the three eigenenergy bands are

$$\lambda_{n=1,2,3}(\boldsymbol{q}) = C_1 + \frac{2C_2}{3}\cos\Big[\frac{1}{3}\arccos\frac{\sqrt{6}C_3}{\sqrt{C_2^3}} + \frac{2n\pi}{3}\Big]. \tag{11}$$

More quantitatively, to order $\boldsymbol{q}^3$, one finds

$$\begin{aligned} C_1(\boldsymbol{q}) &= s(k + \tfrac{1}{4k}\boldsymbol{q}^2 + \tfrac{1}{8k^2}q_y(3q_x^2 - q_y^2)), \\ C_2(\boldsymbol{q}) &= \tfrac{3t_M^2}{2} + \tfrac{3(4k^2+3t_M^2)}{8k^2}\boldsymbol{q}^2 - \tfrac{3(4k^2-9t_M^2)}{16k^3}q_y(3q_x^2 - q_y^2), \\ C_3(\boldsymbol{q}) &= -\tfrac{3t_M^3}{4} + \tfrac{27t_M^2(2sk+t_M)}{16k^2}\boldsymbol{q}^2 + \tfrac{3(8sk^3+27t_M^3)}{32k^3}q_y(3q_x^2 - q_y^2). \end{aligned} \tag{12}$$

Using these expressions, for $t_M < 0$, the three electron bands $E_1 < E_2 < E_3$ read

$$\begin{aligned} E_1(\boldsymbol{q}) &= X(\boldsymbol{q}) - \tfrac{1}{2}[Y_+(\boldsymbol{q}) + \sqrt{Z_+(\boldsymbol{q})}], \\ E_2(\boldsymbol{q}) &= X(\boldsymbol{q}) - \tfrac{1}{2}[Y_+(\boldsymbol{q}) - \sqrt{Z_+(\boldsymbol{q})}], \\ E_3(\boldsymbol{q}) &= X(\boldsymbol{q}) + Y_+(\boldsymbol{q}). \end{aligned} \tag{13}$$

Similarly for the hole bands $H_1 > H_2 > H_3$ one obtains,

$$\begin{aligned} H_1(\boldsymbol{q}) &= -X(\boldsymbol{q}) + Y_-(\boldsymbol{q}), \\ H_2(\boldsymbol{q}) &= -X(\boldsymbol{q}) - \tfrac{1}{2}[Y_-(\boldsymbol{q}) + \sqrt{Z_-(\boldsymbol{q})}], \\ H_3(\boldsymbol{q}) &= -X(\boldsymbol{q}) - \tfrac{1}{2}[Y_-(\boldsymbol{q}) - \sqrt{Z_-(\boldsymbol{q})}], \end{aligned} \tag{14}$$

where

$$\begin{aligned} X(\boldsymbol{q}) &= k + \tfrac{1}{4k}\boldsymbol{q}^2 + \tfrac{1}{8k^2}q_y(3q_x^2 - q_y^2), \\ Y_\pm(\boldsymbol{q}) &= -t_M - \tfrac{(2k+3t_M)}{6t_M k}\boldsymbol{q}^2 + \tfrac{(3t_M \pm 2k)}{18t_M^2 k}q_y(3q_x^2 - q_y^2), \\ Z_\pm(\boldsymbol{q}) &= \tfrac{(3t_M \pm 2k)^2}{4k^2}\boldsymbol{q}^2 + \tfrac{(81t_M^3 - 12k^2 t_M \pm 16k^3)}{24k^3 t_M}q_y(3q_x^2 - q_y^2). \end{aligned} \tag{15}$$

To understand the content of these expressions, it is convenient to consider the limit of very small t_M. In this limit, rewriting $q\tilde{}_{x,y} = q_{x,y}/t_M$ with $|q\tilde{}_{x,y}| \ll 1$ and keeping terms at most of linear order in t_M in the energy bands we can use the simplified expressions

$$\begin{aligned} X(\tilde{\boldsymbol{q}}) &\simeq k, \\ Y_\pm(\tilde{\boldsymbol{q}}) &\simeq -t_M[1 + \tfrac{1}{3}\tilde{\boldsymbol{q}}^2 \pm \tfrac{1}{3}q\tilde{}_y(3q\tilde{}_x^2 - q\tilde{}_y^2)], \\ Z_\pm(\tilde{\boldsymbol{q}}) &\simeq t_M^2[\tilde{\boldsymbol{q}}^2 \pm \tfrac{2}{3}q\tilde{}_y(3q\tilde{}_x^2 - q\tilde{}_y^2)]. \end{aligned} \tag{16}$$

such that we can rewrite the electron and hole bands

$$\begin{aligned} E_1(\tilde{\boldsymbol{q}}) &= k + \tfrac{t_M}{2}[1 + \tfrac{1}{3}\tilde{\boldsymbol{q}}^2 + \tfrac{1}{9}q\tilde{}_y(3q\tilde{}_x^2 - q\tilde{}_y^2) + \sqrt{\tilde{\boldsymbol{q}}^2 + \tfrac{2}{3}q\tilde{}_y(3q\tilde{}_x^2 - q\tilde{}_y^2)}], \\ E_2(\tilde{\boldsymbol{q}}) &= k + \tfrac{t_M}{2}[1 + \tfrac{1}{3}\tilde{\boldsymbol{q}}^2 + \tfrac{1}{9}q\tilde{}_y(3q\tilde{}_x^2 - q\tilde{}_y^2) - \sqrt{\tilde{\boldsymbol{q}}^2 + \tfrac{2}{3}q\tilde{}_y(3q\tilde{}_x^2 - q\tilde{}_y^2)}], \\ E_3(\tilde{\boldsymbol{q}}) &= k - t_M[1 + \tfrac{1}{3}\tilde{\boldsymbol{q}}^2 + \tfrac{1}{9}q\tilde{}_y(3q\tilde{}_x^2 - q\tilde{}_y^2)]. \end{aligned} \tag{17}$$

Similarly for the hole bands $H_1 > H_2 > H_3$ one obtains,

$$\begin{aligned} H_1(\tilde{\boldsymbol{q}}) &= -k - t_M[1 + \tfrac{1}{3}\tilde{\boldsymbol{q}}^2 - \tfrac{1}{9}q\tilde{}_y(3q\tilde{}_x^2 - q\tilde{}_y^2)], \\ H_2(\tilde{\boldsymbol{q}}) &= -k + \tfrac{t_M}{2}[1 + \tfrac{1}{3}\tilde{\boldsymbol{q}}^2 - \tfrac{1}{9}q\tilde{}_y(3q\tilde{}_x^2 - q\tilde{}_y^2) - \sqrt{\tilde{\boldsymbol{q}}^2 - \tfrac{2}{3}q\tilde{}_y(3q\tilde{}_x^2 - q\tilde{}_y^2)}], \\ H_3(\tilde{\boldsymbol{q}}) &= -k + \tfrac{t_M}{2}[1 + \tfrac{1}{3}\tilde{\boldsymbol{q}}^2 - \tfrac{1}{9}q\tilde{}_y(3q\tilde{}_x^2 - q\tilde{}_y^2) + \sqrt{\tilde{\boldsymbol{q}}^2 - \tfrac{2}{3}q\tilde{}_y(3q\tilde{}_x^2 - q\tilde{}_y^2)}]. \end{aligned} \tag{18}$$

The Dirac cones at κ_S (between E_1 and E_2 and betwen H_2 and H_3) have a dispersion relation $\pm|\tilde{q}|$, i.e. they are isotropic and have a velocity $v_{\kappa_S} = 1/|t_M|$.

Expanding $E_2(\boldsymbol{q})$ to quadratic order around the saddle point at $\boldsymbol{q}^* = (0, 0.78t_M)$, one finds

$$E_2(\boldsymbol{q}^* + \boldsymbol{q}) = E_2^* + \alpha_x q_x^2 + \alpha_y q_y^2, \tag{19}$$

with $E_2^* = k + 0.305t_M$, $\alpha_x = -0.888/t_M$ and $\alpha_y = 0.342/t_M$. From these expressions, one deduces that the saddle point energy is shifted by an amount $-0.195t_M$ from the Dirac point at κ_S with energy $E_2(\kappa_S) = k + t_M/2$. This shift is much larger than that of the saddle point in E_1 from the Dirac points at m_S. The saddle point on the E_2 band is also much less anisotropic than the saddle point in E_1 (there is a factor 2.6 between the two curvatures instead of $1/(2t_M)^2 \sim 100$).

Expanding $H_2(\boldsymbol{q})$ to quadratic order around the saddle point at $\boldsymbol{q}^* = (0, -0.78t_M)$, one finds that the curvatures α_x and α_y are the same as for E_2.

Effective parameters

We now discuss the effective parameters of the Dirac cones at m_S (velocities c_x, c_y and geometrical average $v_S \equiv \sqrt{c_x c_y}$ in units of v) and of the saddle points (curvatures $\alpha_x = 1/(2m_{xx})$, $\alpha_y = 1/(2m_{yy})$ and geometrical average $\alpha \equiv \sqrt{|\alpha_x \alpha_y|}$ in units of v/G) in E_1/H_1 close to m_S and in E_2/H_2 close to κ_S. We fit these parameters on the numerically obtained band structure (see Table I). The validity of the quadratic expansion near a saddle point is up to an energy $\varepsilon_c \sim 10^{-2} vG$.

M_B	c_x	c_y	v_S	α_x	α_y	α	αv_S^2	$\lvert t_M \rvert \alpha / v_S^2$
E_1	1	0.1	0.32	-70	1	8.4	0.84	5.4
E_2	"	"	"	16	-5	8.9	0.89	5.7
H_1	1	0.15	0.38	60	-1	7.7	1.16	3.3
H_2	"	"	"	12	-6	8.5	1.3	3.6
pred. E_1/H_1	1	0.13	0.36	∓ 61	± 1	7.8	1	3.9
pred. E_2/H_2	"	"	"	14	-5	8.6	1.1	4.3

M_A	c_x	c_y	v_s	α_x	α_y	α	αv_S^2	$\lvert t_M \rvert \alpha / v_S^2$
E_1	1	0.07	0.26	-150	1	12	0.85	6.1
E_2	"	"	"	25	-7	13.2	0.92	6.6
H_1	1	0.07	0.26	200	-1	14	0.98	7
H_2	"	"	"	23	-10	15	1.1	7.6
pred. E_1/H_1	1	0.07	0.26	∓ 204	± 1	14.3	1	7.1
pred. E_2/H_2	"	"	"	25	-10	15.8	1.1	8.2

TABLE I. Effective parameters for sample M_B with $t_M = -0.064$ (left) and for sample M_A with $t_M = -0.035$ (right). Velocities are in units of v and curvatures in units of v/G.

This agrees well with the analytical predictions for the anisotropic velocities $c_x = 1$ and $c_y = 2|t_M|$ of the Dirac points at m_S and for the curvatures of the saddle points in the bands E_1/H_1 (close to m_S), $\alpha_x = \mp 1/(2t_M)^2$ and $\alpha_y = \pm 1$ (i.e. $\alpha = 0.5/|t_M|$) and in the bands E_2/H_2 (close to κ_S), $\alpha_x = -0.888/t_M$ and $\alpha_y = 0.342/t_M$ (i.e. $\alpha = 0.55/|t_M|$). It means that $v_S^2 = 2|t_M|$, $\alpha = 0.5/|t_M|$ so that $\alpha v_S^2 = 1$. From the two energies t_M and $v_S^2/\alpha = 2m_{eff} v_S^2$, one can form the dimensionless ratio

$$|t_M| \frac{\alpha}{v_S^2} = \frac{1}{4|t_M|}, \tag{20}$$

which is ~ 4 for M_B and ~ 7.5 for M_A. We use this estimate $|t_M| \frac{\alpha}{v_S^2} \sim 4(M_B) - 7.5(M_A)$ repeatedly in the following.

Density of states and susceptibility singularities at a saddle point

In the following we present analytical results on the paramagnetic singularity of the susceptibility at the two types of saddle points encountered in the moiré band structure of graphene discussed above. The first one is the "ordinary" A_1 saddle point, where energy exhibits a maximum along one axis and a minimum along the perpendicular one. The second one is the C_3 saddle point, where the band curvature is zero in all directions. This point is surrounded by three maxima separated by three valleys at 120° angles.

For clarity, we compute in parallel both density of states and susceptibility, whose expressions bear similarities :

$$\rho = \int \delta(\epsilon(\boldsymbol{p}) - \epsilon) \frac{d^2p}{4\pi^2} \tag{21}$$

$$\chi = \int \delta(\epsilon(\boldsymbol{p}) - \epsilon) \chi(p_x, p_y) \frac{d^2p}{4\pi^2} \tag{22}$$

with

$$\chi(p_x, p_y) = \frac{\mu_0 e^2}{12} \left(\frac{\partial^2 \epsilon}{\partial p_x^2} \frac{\partial^2 \epsilon}{\partial p_y^2} - \left(\frac{\partial^2 \epsilon}{\partial p_x \partial p_y} \right)^2 \right) \tag{23}$$

χ is the so-called Landau-Peierls contribution to the susceptibility, neglecting interband effects [3].

DOS and susceptibility singularities at a A_1 saddle point

We consider the simple saddle point in the dispersion relation modeled as :

$$\epsilon(p_x, p_y) = \alpha_x p_x^2 - \alpha_y p_y^2 . \tag{24}$$

α has the dimension of an inverse mass $\alpha = 1/(2m)$. For generality, we consider the anisotropic case relevant for our situation and choose $0 < \alpha_y < \alpha_x$ and we introduce a momentum cutoff p_c. The integrated density of states (DOS) is given by :

$$N(\epsilon) = \frac{1}{4\pi^2} \int dp_x dp_y \tag{25}$$

with the constraint

$$\begin{aligned} 0 < \epsilon(p_x, p_y) < \epsilon \qquad & \text{for } \epsilon > 0 \\ \epsilon < \epsilon(p_x, p_y) < 0 \qquad & \text{for } \epsilon < 0 \end{aligned} \tag{26}$$

After momentum integration and derivation with respect to the energy, the density of states is given by

$$\rho(\epsilon) = \frac{1}{2\pi^2 \sqrt{\alpha_x \alpha_y}} \ln \frac{\sqrt{\alpha_y p_c + \sqrt{\alpha_y p_c^2 + \epsilon}}}{\sqrt{|\epsilon|}} . \tag{27}$$

At energy well below the cutoff $\sqrt{\alpha_y} p_c$, it takes the simple form

$$\rho(\epsilon) = \frac{1}{4\pi^2 \sqrt{\alpha_x \alpha_y}} \ln \frac{4\alpha_y p_c^2}{|\epsilon|} . \tag{28}$$

Within the Landau-Peierls approximation, the susceptibility is obtained from a similar calculation with an extra factor $\chi(p_x, p_y) = (\mu_0 e^2/3)\alpha_x \alpha_y$, leading to:

$$\chi(\epsilon) = \frac{\mu_0 e^2}{12\pi^2} \sqrt{\alpha_y \alpha_x} \ln \frac{4\alpha_y p_c^2}{|\epsilon|} \tag{29}$$

DOS and susceptibility singularities at a C_3 saddle point

The energy varies as a cubic function of p_x and p_y, which is convenient to parametrize in polar coordinates as:

$$\epsilon(p_x, p_y) = \beta \left(p_x^3 - 3 p_x p_y^2 \right) \equiv \beta p^3 \cos 3\vartheta \tag{30}$$

with an energy cutoff $\epsilon_c = \beta p_c^3$. With integration regions constrained by eq. 26, the integrated DOS is given by

$$N(\epsilon) = \frac{6}{4\pi^2} \int_{\beta p^3 \cos 3\vartheta < \epsilon} d^2 p = \frac{3}{4\pi^2} \left(\frac{\epsilon}{\beta} \right)^{2/3} \int_0^{\pi/6} \frac{d\vartheta}{(\cos 3\vartheta)^{2/3}} \tag{31}$$

The integral converges and yields: $\sqrt{\pi} \Gamma(7/6)/\Gamma(2/3) = 1.214$, so that we get finally for the DOS :

$$\rho(\epsilon) = \frac{C}{\beta^{2/3} |\epsilon|^{1/3}} \tag{32}$$

with $C = 0.0615$.

For the integrated susceptibility $X(\epsilon)$, the integrand has a multiplicative term in $3\mu_0 e^2 \theta^2 p^2$. This yields in polar coordinates:

$$X(\epsilon) = \frac{9}{2\pi^2}\mu_0 \mathbb{C}^2 \theta^2 \int_0^{\vartheta_c} d\vartheta \int_{\theta p^3 \cos 3\vartheta < \epsilon} p^3\, dp\,. \tag{33}$$

Integrating over p with the condition $\theta p^3 \cos 3\vartheta < \epsilon$, leads to:

$$X(\epsilon) = \frac{9}{8\pi^2}\mu_0 e^2 \theta^{3/2} \epsilon^{4/3} \int_0^{\vartheta_c} \frac{d\vartheta}{(\cos 3\vartheta)^{4/3}} \tag{34}$$

with the cutoff $\vartheta_c \,' \pi/6 - \epsilon/(3\epsilon_c)$. We use the expansion :

$$\int_0^{\pi/6-x} \frac{d\vartheta}{(\cos 3\vartheta)^{4/3}} \quad \underset{x\to 0}{\longrightarrow} \quad \frac{1}{(3x)^{1/3}} - b\,. \tag{35}$$

with $b = \sqrt{\pi}\Gamma(5/6)/\Gamma(1/3) \;\blacksquare\; 0.747$ and we find

$$X(\epsilon) = \frac{9\mu_0 e^2}{8\pi^2}\,\theta^{2/3}\epsilon^{4/3}\left[\frac{\epsilon_c^{1/3}}{\epsilon^{1/3}} - b\right] \tag{36}$$

The susceptibility at energy ϵ is obtained by derivation and reads:

$$\chi(\epsilon) = \frac{9}{8\pi^2}\mu_0\, e^2\, \theta^{2/3}\,(\epsilon_c^{1/3} - c|\epsilon|^{1/3}) \tag{37}$$

with $c = 4b/3 \,' 1$. The susceptibility is therefore finite at its maximum and depends on the cut-off ϵ_c.

Gaussian broadening

The effect of disorder can be accounted for by a gaussian distribution of chemical potentials of width σ. The susceptibility becomes

$$\chi_\sigma(\mu) = \int \chi(\mu')\, P(\mu - \mu')d\mu' \tag{38}$$

with

$$P(\mu) = \frac{e^{\frac{-\mu^2}{2\sigma^2}}}{\sqrt{2\pi\sigma}} \tag{39}$$

The logarithmic singularity in eqs.(28,29) is smoothed according to:

$$\ln|\epsilon| \longrightarrow \int \ln|\mu'|\frac{e^{\frac{-(\mu-\mu')^2}{2\sigma^2}}}{\sqrt{2\pi}\sigma}d\mu' \tag{40}$$

For $\mu = 0$, the divergence $1/\ln|\epsilon|$ is cut as $1/\ln A\sigma$ with $A = \sqrt{\frac{1}{2}e^{-\gamma/2}} \;\blacksquare\; 0.53$ and $\gamma = 0.577...$ is the Euler constant.

Similar calculation for the C_3 singularity yields:

$$|\epsilon|^{1/3} \longrightarrow \int |\mu'|^{1/3}\frac{e^{\frac{-(\mu-\mu')^2}{2\sigma^2}}}{\sqrt{2\pi}\sigma}d\mu' \tag{41}$$

For $\mu = 0$, one finds that :

$$\chi(\mu = 0) = \frac{9}{8\pi^2}\mu_0\, e^2\, \theta^{2/3}\,(\epsilon_c^{1/3} - d\sigma^{1/3}) \tag{42}$$

with $d = c\, 2^{1/6}\Gamma(2/3)/\sqrt{\pi} \;\blacksquare\; 0.854$.

Orbital susceptibility and comparison with experimental data

One important parameter is the energy width σ_s of the satellite Dirac peak which limits the amplitude of the susceptibility peaks. In Fig.11 in section II.C, we show how to extract σ_s from the gate voltage derivative of the magnetisation $M'(V_g) \propto \mu M'(\mu)$. The spacing between the maximum and the minimum of $M'(\mu)$ fitted by the derivative of a gaussian centered at μ_S around μ yields $2\sigma_S = 9 \pm 1$ meV for both samples. In the following for quantitative comparisons we mostly focus on the sample M_B, with the largest moiré potential period and amplitude, for which the data is the most reliable due to the larger energy spacing between paramagnetic and diamagnetic peaks.

Secondary Dirac peak versus main Dirac peak

The ratio of susceptibility peaks at the sDP χ_S and the main Dirac peak χ_M reads:

$$r \equiv \frac{\chi_S}{\chi_M} = \frac{3v_S^2/\sigma_S}{v^2/\sigma_0} = 3 \times 2|t_M| \times \frac{\sigma_0}{\sigma_S} = 3 \times 2(0.035 - 0.064) \times 1.5 \approx 0.32(M_A) - 0.58(M_B) \quad (43)$$

Experimentally, $\sigma_0 = 80$ K $= 6.9$ meV, and $\sigma_S = 4.5$ meV so that $\sigma_S/|t_M| \sim 0.2(M_B) - 0.3(M_A)$.

The measured ratio is $r = 0.33 \pm 0.1$, for M_B which is of the order but 1.7 times lower than the expected value given above, we show in the next section that this disagreement is probably due to an underestimation of the diamagnetic peak χ_S very close to the inner Vignale paramagnetic peak (on the low doping side). The same calculation gives $r = 0.32$ for M_A which is also larger than the measured value of the order of 0.1 with a very large error bar (see tables in section II).

Vignale paramagnetism versus McClure diamagnetism

The Vignale paramagnetic susceptibility $\chi_V \sim \alpha \ln(\epsilon_c/\sigma_s)$ and the McClure diamagnetic susceptibility (at the sDP) $\chi_S \sim -v_S^2/\sigma_s$, where σ_s is the disorder broadening. Their ratio (up to numerical factors) is

$$\frac{\chi_V}{|\chi_S|} \sim \frac{\alpha}{v_S^2}\sigma_s \ln(\epsilon_c/\sigma_s) \sim |t_M|\frac{\alpha}{v_S^2} \times \frac{\sigma_s}{|t_M|} \approx (4 - 7.5) \times (0.1 - 0.15) \approx 0.4(M_B) - 1.1(M_A). \quad (44)$$

This is just an order of magnitude estimate. However, for the precise ratio between the maximas of the derivative χ', we find:

$$r_{VD} = \frac{\chi_V}{|\chi'_S|} \approx \frac{6}{3} \times \frac{0.0065\alpha/\sigma_s}{0.013v_S^2/\sigma_S^2} \approx \frac{\alpha}{v_S^2}\sigma_s = |t_M|\frac{\alpha}{v_S^2} \times \frac{\sigma_s}{|t_M|} \approx 0.4(M_B) - 1.1(M_A), \quad (45)$$

where $6/3$ accounts for the 6 saddle points versus the 3 sDPs and $\sigma_s/|t_M| \sim 0.1$. The relative magnitude of the orbital paramagnetism and diamagnetism for the moiré band structure is therefore given by the following important dimensionless ratio

$$\frac{\alpha}{v_S^2}\sigma_s = \frac{vG}{4t_M}\frac{\sigma_s}{t_M}, \quad (46)$$

It is interesting to note that r_{VD} decreases with $1/G \propto a_M$ and t_M. This is why it is expected to be larger for the M_A sample than M_B in agreement with our experimental results. In particular all paramagnetic peaks on bands E_1, H_2 and E_2 are visible for M_A. A different behavior is observed for the M_B sample: saddle points on the E_1 and H_1 bands are nearly not detectable whereas instead paramagnetic peaks are clearly observed on the E_2,H_2 bands and the ratio $r_{VD} = 0.8 \pm 0.2, 0.35 \pm 0.15$ can be estimated, see section II below. A similar quantitative estimation is delicate on M_A: on the one hand the amplitude of the diamagnetic peak at sDPs is difficult to estimate and on the other hand the large doping region of saddle points in the E_2 and H_2 bands correspond to large gate voltages of the order of $\pm 20V$ for which the insulating properties of the hBN top layer become not reliable and therefore experimental data are not reproducible. This explains the large error bars in Table II of section II.

Vignale orbital paramagnetism versus Pauli spin paramagnetism at the saddle points

Vignale's susceptibility is $\chi_V = \frac{\alpha^2}{3}\rho(\epsilon)$ where ρ is the DoS and we have taken $\mu_0 \equiv 1$ and $e \equiv 1$. Pauli's susceptibility is $\chi_P = \frac{g}{2}\mu_B^2\rho(\epsilon)$ with the Bohr magneton $\mu_B = \frac{ek}{2m_e} = \frac{1}{2m_e}$, where m_e is the bare electron mass and $g \approx 2$ for graphene. Their ratio is:

$$\frac{\chi_V}{\chi_P} = \frac{\alpha^2/3}{\mu_B^2} = \frac{4}{3}\alpha^2 m_e^2 = \frac{1}{3}\left(\frac{m_e}{m_{eff}}\right)^2 = \frac{1}{3u_0^2}\left(\frac{m_e v}{kG}\right)^2 \approx 14000(M_B) - 27000(M_A) \sim 10^4. \quad (47)$$

In other words, since a typical effective mass at the saddle point of the moiré band structure is $m_{eff} = 1/(2\alpha) \sim 4.10^{-3} m_e$ (i.e. $m_e/m_{eff} \sim 200$), the spin paramagnetism is completely negligible compared to the orbital paramagnetism. We note that $\frac{1}{3}\left(\frac{m_e}{m_{eff}}\right)^2$ is the famous ratio between orbital and spin magnetic susceptibility usually discussed near a band edge when comparing Landau diamagnetism and Pauli paramagnetism.

MORE DETAILS ON EXPERIMENTAL RESULTS.

Fabrication and characterization of the investigated samples.

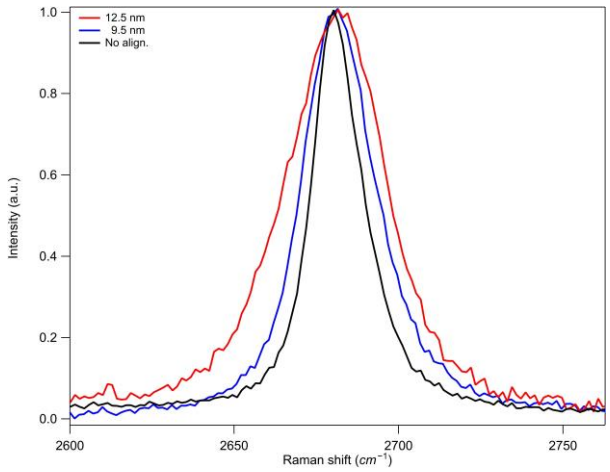

FIG. 6. Signatures of the moiré potential on the width of the Raman 2D peak.

We start from a selected exfoliated graphene monolayer with a hBN flake. We first identified long straight edges in both graphene and hBN layers. These edges follow the crystallographic axes of each honey-comb lattice. Therefore, by aligning these straight edges, one has equal probability that graphene and hBN are aligned or that their respective alignment form a 30° angle. In order to guarantee the alignment, two different methods were followed for the two samples M_A and M_B investigated. For sample M_B, a flake of graphene with a long straight edge of about $45\mu m$ long was cut in three parts of roughly 20, 5 and $20\mu m$ respectively. The first part was aligned and picked-up with a straight edge of a big flake of hBN. Then covered by a bottom misaligned hBN. The second and third parts were rotated with an angle of 30° with respect to the hBN edge, picked up with another part of the same top hBN flake and finally dropped onto a misaligned hBN. Raman spectroscopy measurements allowed us to determine which of the two samples is the one with the largest moiré constant by measuring the width of the 2D peak. This sample was selected and deposited on the top of the GMRs based magnetisation detector, using the standard dry transfer techniques.

In the case of sample M_A, a large hBN flake was cut into two parts along one main crystallographic edge (this was done by opening a narrow slit though the hBN flake using electron-beam lithography followed by reactive ion etching) A single graphene flake was then aligned along the straight edge of one of the halves of the hBN flake, and encapsulated beween this part and the other half previously rotated by 30°. The presence of a long-range moiré pattern, was confirmed by Raman spectroscopy associated this changes with For both samples Raman experiments enabled us to determine the moiré lattice parameters. According to [4] (see also [5]), the full width at half maximum (FWHM) of the 2D peak of the Raman spectrum of graphene is very sensitive to the folding of the phonon structure due to the moiré pattern. This creates copies of the 2D peaks with small differences in their Raman shift. This is reflected by an increase of the FWHM of the 2D peak which varies linearly with the superlattice period, a_M leading to the relation $\mathrm{FWHM}_{2D} = 2.7 a_M + 0.77$.

From Fig. 6, we found the FWHM of the D peak to be $26.5 cm^{-1}$ for M_A sample and $34.9 cm^{-1}$ for M_B. From these values, using the relation given above relating the width of the Raman D peak to the moiré period, we can deduce for the 2 samples A and B, $a_M = 9.5nm$ and $12.5nm$ nm as well the twist angle ϑ between the hexagonal lattices of graphene and hBN acording to the relation $a_M = (1+\delta)a_G/(\sqrt{2(1+\delta)[1 - \cos\vartheta] + \delta^2})$, where $\delta = 0.017$ is the ratio between graphene and hBN lattice constants). We find $\vartheta_A = 1.1°$ and $\vartheta_B = 0.6°$.

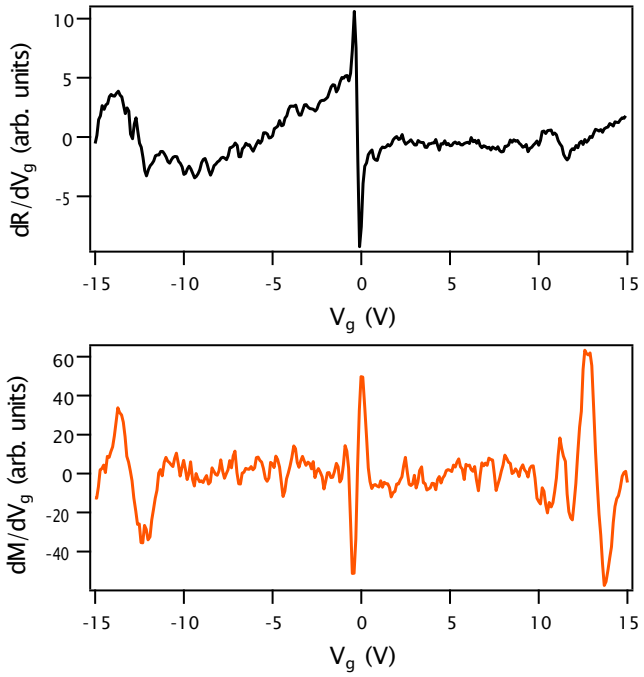

FIG. 7. Top: derivative of the resistance as a function of the gate voltage for sample M_B. Bottom: derivative of the magnetization as a function of the gate voltage for the same sample.

The period of the moiré lattices coincides with those expected from the magnetisation curves. As shown in Fig.3 of the main paper, the diamagnetic peaks are located very close to the doping (or V_g) at which the density is equal to 4 electrons (or holes) per moiré-unit cell. In contrast, transport measurements show a satellite peak at a smaller density. Since the geometry of the two experiments differ, we may be seeing a slightly different effective moiré period(of about 0.5nm) in each experiment. This difference might be caused by local strain. In any case, the difference in the position in doping between magnetisation and resistance measurements can be explained by considering the error bars of the calibration of the moiré-length/FWHM relation in [4].

Effect of the gate voltage modulation

We first present in Fig.7 the gate voltage derivative of the resistance of sample M_B. This allows us to directly compare the positions (in gate voltage) of the main and secondary Dirac peaks with the corresponding diamagnetic peaks. We observe antisymmetric peaks both in the resistance and the magnetisation at the Dirac peak. At higher doping, we see the derivative of the secondary Dirac peaks in the resistance . In magnetization, we observe both seconday McClure peaks and paramagnetic peaks. When this magnetization curve is integrated, it gives the curves shown in Fig.3 of the main text for different values of magnetic field. From this data taken at different values of magnetic field between 0.1 and 0.2 T one can appreciate the reproducibility of the intensity and positions of the diamagnetic secondary McClure peak and the outer paramagnetic peaks, whereas the inner paramagnetic peaks are nearly invisible at low field.

We now consider on the same data the effects of modulation and integration. Figure 8 compares the integrated curve of data in 7 after subtraction of a linear background, with data taken obtained for a smaller range of gate voltage and with a smaller modulation. We can notice that the higher modulation allows us to obtain a smoother curve with less noise, but certain structures get rounded in a non-negligible way. We also investigated the effect of the range of gate voltage along which integration is performed. We compare the curves obtained after integrating the data in the whole range of V_g investigated (between -15 to 15V) with the curve obtained after splitting the data in 3 pieces along the V_g axis. Whereas the main magnetization peaks are unchanged, we find that integrating over the full range of gate voltage generates an extra negative contribution on the magnetisation which is not seen when the integration range is reduced to 10V.

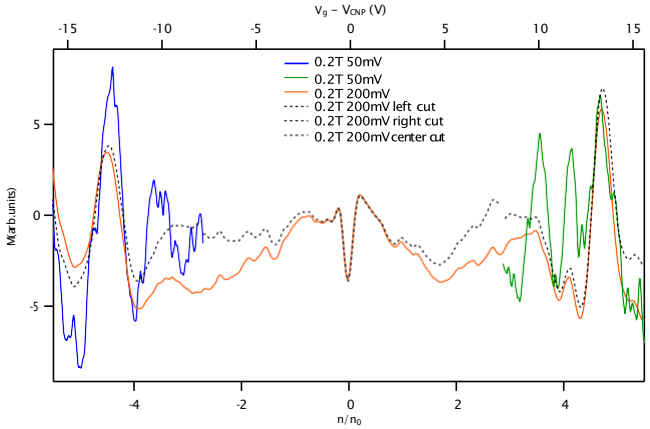

FIG. 8. Comparison of the magnetization of sample M_B, with different gate voltage modulations, for an external field of 0.2 T. In orange, the curve for 200 millivolt integrated in the full range of gate voltage investigated (-15.5 to 15.5 volt), see Fig.3 in the main text. In blue, the electron's (left) sDP region measured at 50 millivolt and integrated in a range between -16 to -8 volt. In green, the hole's (right) sDP region measured with 50 millivolt gate voltage modulation and integrated in a range between 8 to 16 volt. In dashed black, the integration of the data obtained with 200 millivolt gate voltage modulation was split into 3 regions: left $(-16\,;-8)$ volt, center $(-8\,;8)$ volt and right $(8\,;16)$ volt.

Additional data for different values of magnetic field

We present here magnetisation data not shown in the main part of the paper. Magnetisation is expressed in units of the magnetic field detected on the GMR sensor. For the measurements on M_B the experimental conditions (dc current though the GMR detector as well as gate voltage modulation) were chosen in order to optimize the quality of the signal. In particular the large gate voltage modulations tend to washout the main Dirac peak as well as dHvA oscillations. One can identify the diamagnetic satellite peaks which are clearly split on the electron side as well as the outer paramagnetic peaks. Similar data is also shown on M_A in a smaller range of gate voltage focusing on the regions in the vicinity of satellite Dirac points both in hole and electron doping sides. In both cases paramagnetic peaks on both sides of the diamagnetic satellite peaks are visible with a more complex behavior with split peaks on the hole side which will be discussed below.

Finally, in Fig.11, we explain how we determined σ_S, the amplitude of disorder around the satellite Dirac peaks of the hBN/Graphene bilayer of sample M_B. The value of σ_S, is obtained from the distance in energy between maxima and minima of the chemical potential derivative of the secondary diamagnetic peaks as explained above.

Similar analysis on sample M_A gives a similar value of σ_S = 5.0 ± 0.5 millielectronvolt.

Characteristics of the susceptibility peaks around the satellite Dirac points in comparison with numerical calculations

In the following we present a more detailed analysis of the experimental data, than to what is done in the main paper, in comparison with the band structure ans its analysis depicted in the previous section. For each sample investigated this analysis relies on only 2 adjustable parameters. The first one is the energy width of the peaks estimated above and the second one is the amplitude of the moiré potential t_M determined from the relative positions of the satellite Dirac points and the positions of those large doping paramagnetic peaks clearly which can be identified. The next step is then to understand the amplitudes of the different peaks observed. In tables II and III, we summarize the parameters extracted and used for the comparisons between experimental and theoretical data. Since our model does not take into account the electron-hole asymmetry in the experiment, one has to consider that the parameter t_M is an average between the values which could be deduced fitting only the hole or the electron side of the data shown in Fig.4. $\Delta\mu_{i\,E,H} = |\mu_{para,i} - \mu_{dia,i}|_{E,H}$ (in millielectronvolt) are obtained from the distance in energy between the chemical potentials of the paramagnetic and corresponding diamagnetic peaks for each band (when they are visible), the rather large error bar comes from the width σ_S which is not negligible compared to their spacing. The subindex $i = 1, 2$ is related to the considered band : $E_{1,2}$ or $H_{1,2}$. The amplitudes of the magnetization M_i (in nanotesla) are measured directly from the magnetization data. All values are obtained at an applied field of 0.2 tesla. From the values given in these tables, we can calculate the experimental value of $\frac{\chi_V}{|\chi_S|}$. These ratios are of the same order of magnitude than the theoretical ratio $\frac{\chi_V}{|\chi_S|}$ for both samples discussed in the previous section.

In the following we show on two examples that it is possible to go further and reproduce the shape of the magnetic singularities on the electron side considering the contribution of *both diamagnetic peaks at Dirac points* m_S and κ_S together with the

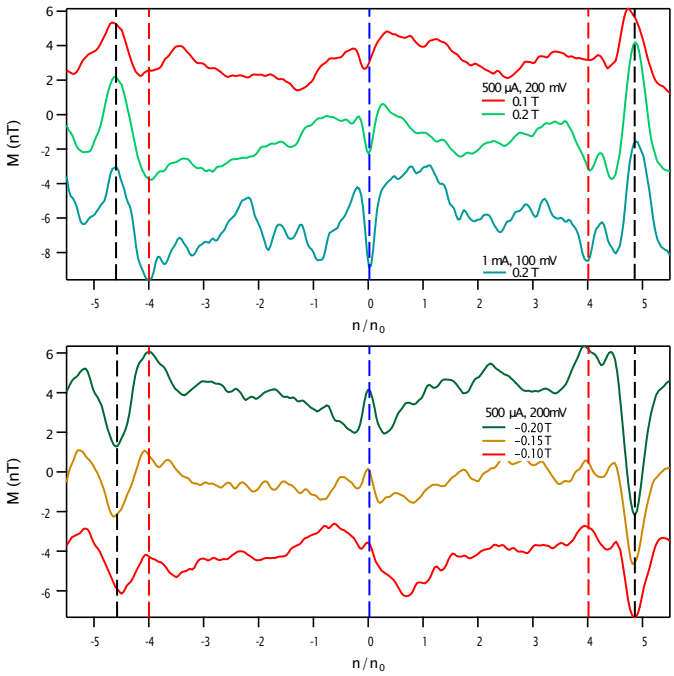

FIG. 9. Magnetization as a function of density (normalized by n_0) for sample M_B for a set of additional low fields, different from the fields discussed in the main text. The top plot shows positive fields and the bottom plot shows negative fields. Curves have been shifted in the vertical axis for better visualization. For each curve the dc current though the GMR sensor is indicated as well as the amplitude of modulation. Dashed vertical line indicate the paramagnetic Vignale peaks (black) and the diamagnetic McClure peaks.

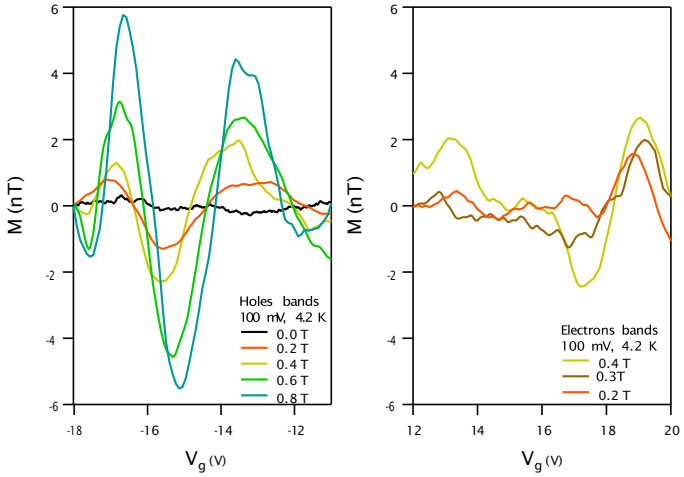

FIG. 10. Magnetization as a function of gate voltage for sample M_A for different magnetic fields. The data shows only the vicinity of the secondary Dirac peaks in the hole and electron doping sides.

M_A	$\Delta\mu_1$	$\Delta\mu_2$	σ_S	$\lvert M_{CNP}\rvert$	$\lvert M_{sDP}\rvert$	$\lvert M_{para-1}\rvert$	$\lvert M_{para-2}\rvert$
$E_{1,2}$	10 ± 10	10 ± 2	4.8	15	1 ± 0.5	0.5 ± 0.5	1 ± 0.5
$H_{1,2}$	5 ± 5	12 ± 3	5	"	1.6 ± 0.5	1 ± 0.5	2 ± 0.5

TABLE II. Experimental parameters for sample M_A. $\Delta\mu_i = |\mu_{para,i} - \mu_{dia,i}|$ and σ_S are given in millielectronvolt . The amplitudes of the magnetization at charge neutrality point M_{CNP}, at the secondary Dirac points M_{sDP}, and the paramagnetic peaks $M_{para-1,2}$ are given in nanotesla. The large errors bars come the small energy separation between these peaks compared to their width.

paramagnetic sigularities at the saddle points which tend to compensate the diamagnetic ones. In particular we see that the

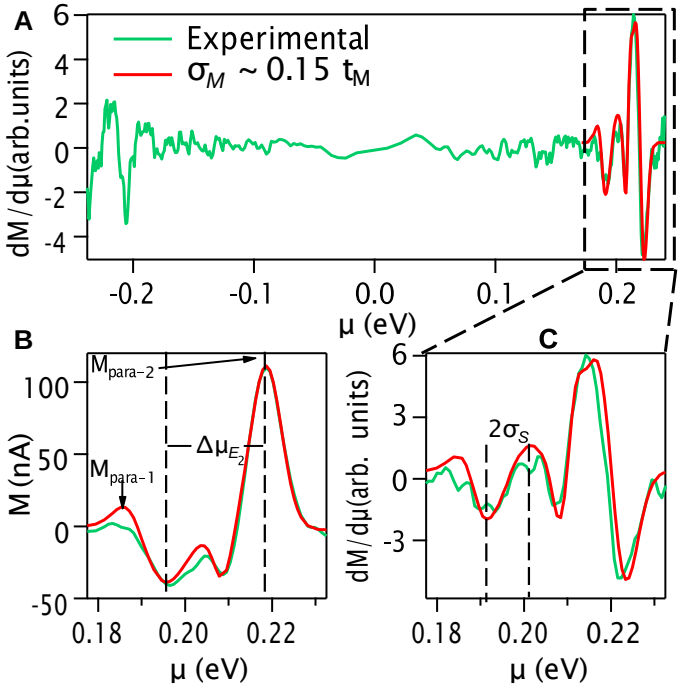

FIG. 11. (A) In green, derivative of the magnetization as a function of the chemical potential for sample M_B. In red, the signal is fit with the derivative of 4 gaussian peaks (2 paramagnetic and 2 diamagnetic) centered respectively around the saddle points and the split satellite Dirac peak. (B) Integral of the zone in a dashed rectangle in figure (A) as well as the integral of the fit. (C) Zoom of the rectangle zone in figure (A). From the fit of the experimental data we obtain $\sigma_S = 4.5 \pm 0.5$ millielectronvolt.

M_B	$\Delta\mu_1$	$\Delta\mu_2$	σ_S	$\lvert M_{CNP} \rvert$	$\lvert M_{sDP} \rvert$	$\lvert M_{para-1} \rvert$	$\lvert M_{para-2} \rvert$
$E_{1,2}$	N.A.	23	4	5.6	1.8	N.A.	3.3
$H_{1,2}$	N.A.	14	5	"	1.7	N.A.	1.7

TABLE III. Experimental parameters for sample M_B. $\Delta\mu_i = |\mu_{para,i} - \mu_{dia,i}|$ and σ_S are given in millielectronvolt . The amplitudes of the magnetization at charge neutrality point M_{CNP}, at the secondary Dirac points M_{sDP}, and the paramagnetic peaks $M_{para-1,2}$ are given in nanotesla.

proximity between the low doping saddle point and m_S has a different manifestation on both samples. In the case of M_B the low doping(inner) paramagnetic Vignale peak is largely reduced by the diamagnetic peak of larger amplitude. This is why it is strongly depressed whereas the diamagnetic peak is only reduced by a factor two. On the other hand, in the case of M_A the inner paramagnetic peak is still visible, due to its greater amplitude compared to the diamagnetic one at m_S, which is in contrast strongly depressed whereas the diamagnetic peak at K_S is clearly visible. We finally note that the outer paramagnetic peak is clearly visible on both samples.

[1] Matthew Yankowitz, Jiamin Xue, Daniel Cormode, Javier D. Sanchez-Yamagishi, K. Watanabe, T. Taniguchi, Pablo Jarillo-Herrero, Philippe Jacquod and Brian J. LeRoy, "Emergence of superlattice Dirac points in graphene on hexagonal boron nitride", Nature Phys. **8**, 382 (2012).

[2] J. R. Wallbank, A. A. Patel, M. Mucha-Kruczynski, A. K. Geim, and V. I. Fal'ko, "Generic miniband structure of graphene on a hexagonal substrate", Phys. Rev. B **87**, 245408 (2013).

[3] R. Peierls "On the Theory of Diamagnetism of Conduction Electrons". Zeitschrift für Physik **80**,763 (1933).

[4] Ribeiro-Palau, R., Zhang, C., Watanabe, K., Taniguchi, T., Hone, J., Dean, C. R. Science, **361**(6403), 690-693 (2018).

[5] A. Eckmann, J. Park, H. Yang, D. Elias, A. S. Mayorov, G. Yu, R. Jalil, K. S. Novoselov, R. V. Gorbachev, M. Lazzeri, A. K. Geim, C. Casiraghi *Nano Lett.* **13**(11), 5242-5246 (2013).

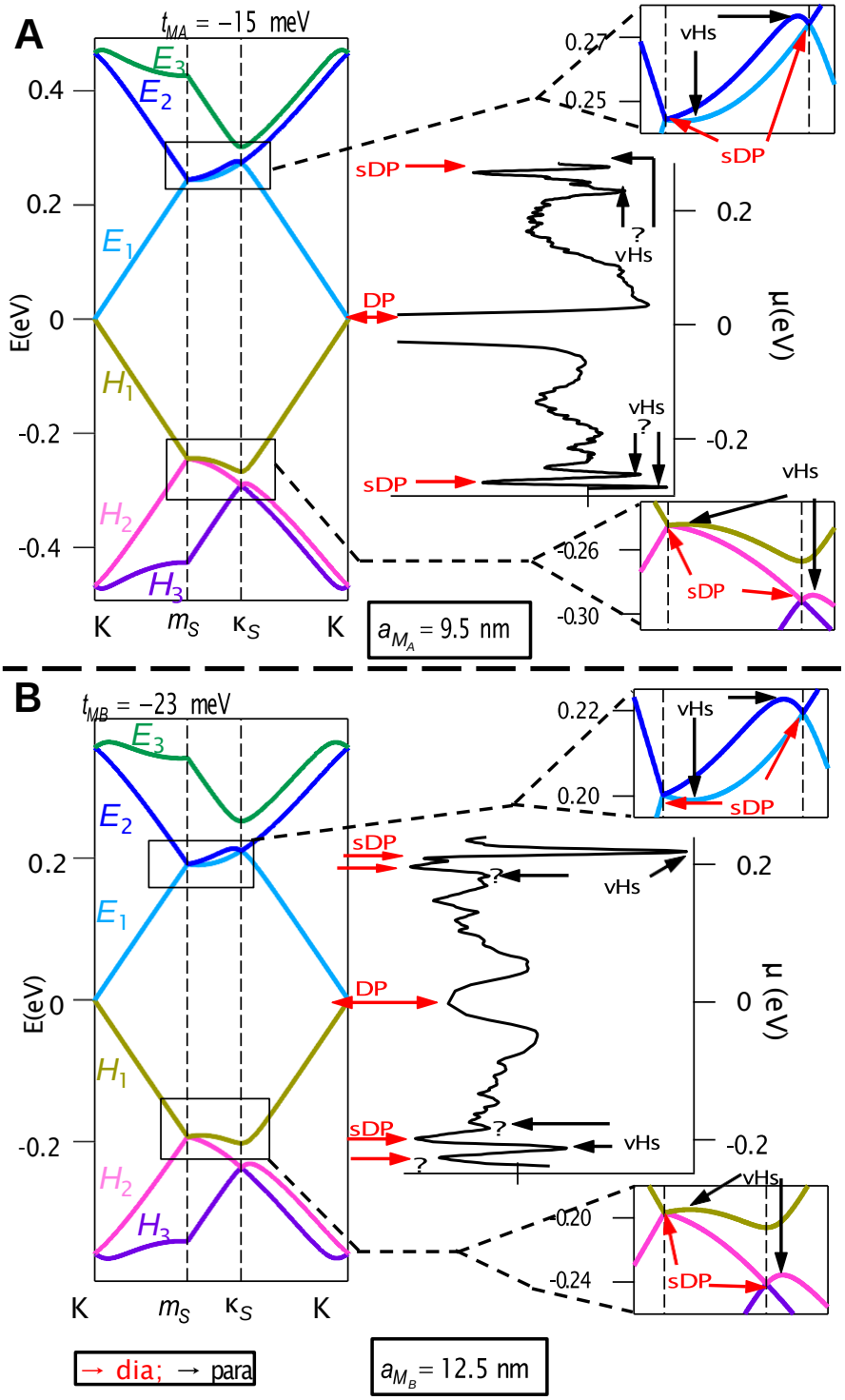

FIG. 12. **(A)** and **(B)** Magnetisation data on samples M_B and M_A measured at 0.2 T function of the chemical potential in eV. (We note that due to the V_g dependence, the energy width of satellite Dirac points is smaller than the width of the main Dirac point.) The difference between the chemical potential of the sDP of the samples M_B and M_A is directly related to their different periodicity a_M = 12.5 nm and 9.5 nm respectively. Experimental data are compared to cuts along the $K, \kappa_S, \kappa_S, m_S, m_S, K$ axis of the moiré band structure calculated for different values of t_M matching the position of the observed diamagnetic peaks (red arrows) and paramagnetic peaks (black arrows) of both samples.

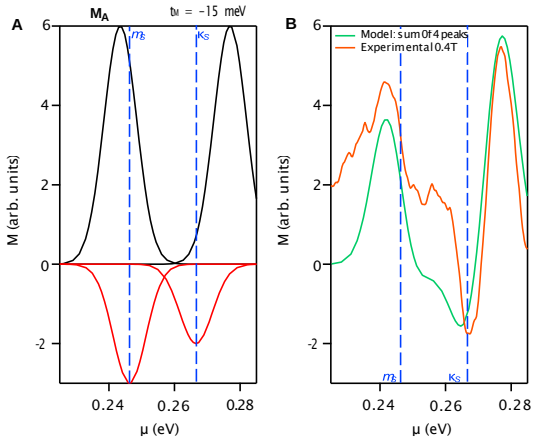

FIG. 13. **(A)** Illustration of how diamagnetic and paramagnetic responses combine on the H_1 band for the M_A sample. We consider four similar separated peaks (two paramagnetic (black) and two diamagnetic (red)), centered at the energies determined by the band structure shown in 12A. These peaks have been constructed as gaussians with σ_S = 5meV. Their amplitudes are determined by taking into account their multiplicity and the ratio $\chi_V/|\chi_S|$ = 1 from the estimations in section I. **(B)** Comparison between the experimental data (orange) and the sum (green) of the 4 peaks in **(A)**.

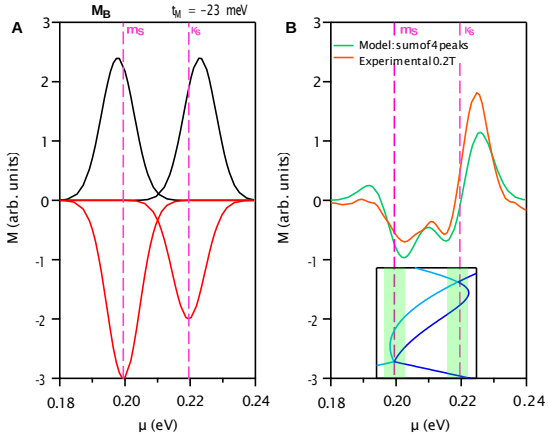

FIG. 14. **(A)**Illustration of how diamagnetic and paramagnetic responses combine on the H_1 band for the M_B sample. We consider four similar separated peaks (two paramagnetic (black) and two diamagnetic (red))centered at the energies determined by the band structure in 12B. These peaks have been constructed as gaussians with σ_S = 5meV. Their amplitudes are determined by taking into account their multiplicity and the ratio $\chi_V/|\chi_S|$ = 0.4 from the etimation in section I. **(B)** Comparison between the experimental data (orange) and the sum (green) of the 4 peaks in **(A)**. The inset shows the related zone of the band structure, and the green area shows the zone where the Dirac peak is broadened.